

Article

A Polymer-Binder-Free Approach to Creating Functional LiFePO₄ Cathodes by Organic Ionic Plastic Crystal-Derived Ion-Conductive Binders

Daniela M. Josepetti ^{1,†}, Maria Forsyth ^{1,2} , Patrick C. Howlett ^{1,2} and Hiroyuki Ueda ^{1,2,*} 

¹ Institute for Frontier Materials (IFM), Deakin University, 221 Burwood Highway, Burwood 3125, Australia; maria.forsyth@deakin.edu.au (M.F.); patrick.howlett@deakin.edu.au (P.C.H.)

² Battery Research and Innovation Hub, Deakin University, 5/154 Highbury Road, Burwood 3125, Australia

* Correspondence: hueda@deakin.edu.au

† Pôle Chimie Balard Recherche, 1919 Route de Mende, 34293 Montpellier, France.

Abstract: Lithium-ion batteries are a promising technology to promote the phase-out of fossil fuel vehicles. Increasing efforts are focused on improving their energy density and safety by replacing current materials with more efficient and safer alternatives. In this context, binary composites of organic ionic plastic crystals (O IPCs) and lithium salts show promise due to their impressive mechanical properties and ionic conductivity. Taking advantage of this, the present paper substitutes the commercial non-electrochemically active binder with an OIPC component, *N*-ethyl-*N*-methylpyrrolidinium bis(fluorosulfonyl)imide ([C₂mpyr][FSI]), in combination with LiFSI. Slurry-formulation experiments revealed that varying the new binder's composition allows the production of diverse LiFePO₄ (LFP) cathodes via the conventional fabrication process. Large amounts of OIPC–lithium salt mixtures in the composition yielded thick electrodes with expected nominal areal capacities of up to 3.74 mAh/cm², where the balanced composition with a reduced Li⁺ concentration can demonstrate >1.5 mAh/cm² at 0.1C. Lowering the amount of these ion-conductive binders enabled LFP cathodes to perform effectively under fast cycling conditions at a C-rate as high as 2C. Preliminary battery tests with a limited Li⁺ source demonstrated the feasibility of full-cell operation without using the lithium-metal anode. This work paves the way for developing advanced rechargeable batteries using OIPC-based ion-conductive binders for a wide range of applications.



Academic Editor: Hirotoshi Yamada

Received: 16 November 2024

Revised: 9 December 2024

Accepted: 18 December 2024

Published: 24 December 2024

Citation: Josepetti, D.M.; Forsyth, M.;

Howlett, P.C.; Ueda, H. A

Polymer-Binder-Free Approach to

Creating Functional LiFePO₄

Cathodes by Organic Ionic Plastic

Crystal-Derived Ion-Conductive

Binders. *Batteries* **2025**, *11*, 3.

[https://doi.org/10.3390/](https://doi.org/10.3390/batteries11010003)

batteries11010003

Copyright: © 2024 by the authors.

Licensee MDPI, Basel, Switzerland.

This article is an open access article distributed under the terms and conditions of the Creative Commons Attribution (CC BY) license

(<https://creativecommons.org/licenses/by/4.0/>).

Keywords: polymer-binder-free cathodes; ion-conductive binders; organic ionic plastic crystals; ionic liquids; lithium metal batteries; rechargeable batteries; lithium iron(II) phosphate; composite cathodes

1. Introduction

The development of rechargeable batteries can address the increasing demand for low-emission greenhouse gas vehicles and mobile devices with extended operational duration (while unplugged from electricity) [1]. In fact, lithium-ion batteries (LIBs) are already responsible for outstanding progress in portable electronics and electric cars in terms of energy autonomy and durability [2]. This battery technology, when compared with other commercial rechargeable batteries, exhibits a relatively high energy density, low self-discharge, and low memory effect [3–6]. On the other hand, the current LIBs have approached their theoretical capacities sufficiently [7,8], which limits the continuous improvement of their energy density unless their cell chemistries are changed, and other issues such as environmental and safety concerns hinder their prevalent use [9].

In that sense, the evaluation of new materials for advanced LIBs is appealing because it could offer a solution to some of these drawbacks. One strategy to improve a battery's performance is to reduce electrochemically non-functional materials in the electrode formulation, such as the binder. The most employed commercial binder is poly(vinylidene fluoride) (PVDF), primarily due to its high electrochemical stability [10]. However, PVDF in typical LIB electrodes is added solely to hold the electrode components together, and its electrical conductivity is almost negligible (i.e., $<10^{-10}$ S cm $^{-1}$ at room temperature [11]). Therefore, reducing the weight ratio of a polymer binder in an electrode would provide the electrode with a higher electrical conductivity [12–14], which often sacrifices the mechanical strength of the electrode [12,13,15]. Alternatively, replacing the non-conductive binder with an ion-conductive one is expected to improve the electrochemical performance of electrodes [16–19], while maintaining the necessary mechanical stability of the electrodes for pressing, cell assembly, and battery operation. In addition, this strategy could avoid excess electrolyte solution in the electrodes' pores, thereby reducing the electrolyte solution's required mass. Both consequences potentially lead to an increase in the energy density of the cell. Although such ion-conductive binders have been actively studied for solid-state batteries (as solid polymer electrolytes) [20–22], they have also been demonstrated as useful materials in advanced LIBs using liquid electrolyte solutions [17–19]. Hence, further material exploitation in this direction is worth pursuing to overcome the performance limitations stemming from the conventional non-conductive binders.

One category of ion-conductive materials that shows promise is organic ionic plastic crystals (OIPCs), which are structural analogs of ionic liquids (ILs) but are solids at room temperature [23,24]. OIPCs are typically composed of organic cations that are paired with inorganic anions [25]. Lattice defects and various motions (e.g., rotational, translational, or conformational) of cations and/or anions can cause ion conduction through the 3D lattice of OIPCs, which are beneficial for ions (e.g., Li $^{+}$) to move through the media [23,26]. Additionally, short-range ion motion under stress and the presence of slip-plane defects contribute to the plastic properties of OIPCs. After the breakthrough finding of ionic conductivity improvement by lithium-salt addition to OIPCs [27], these materials have attracted researchers' attention as novel electrolytes for advanced rechargeable batteries [23,28]. Even a small amount of metal-salt addition can result in a significant improvement in ion transport [29]. The formation of a liquid phase in this binary mixture of an OIPC and a metal salt also contributes to the enhanced ion conduction of the medium [27,30]. In some binary mixtures, an increase in the metal salt concentration increases the volume fraction of a liquid phase in the OIPC–metal-salt composite. Interestingly, these binary mixtures often maintain a solid phase until a certain level of metal ion inclusion [31], after which an IL is formed.

Because of such promising ion-conduction properties of OIPC electrolytes, they have been studied as solid electrolyte membranes for solid-state batteries [23,32]. In recent years, they have also been used as additional integrated ion-conduction pathways in solid-state electrodes [33–39]. These studies have demonstrated the huge potential of OIPC electrolytes as functional ion-conductive materials for advanced rechargeable batteries. As OIPC electrolytes are non-volatile and non-flammable materials like ILs, their use in rechargeable batteries is advantageous for addressing safety issues [40]. This could potentially offer the same preferred features as ILs in device operation; for instance, highly Li $^{+}$ -concentrated ILs have shown promising results in terms of improved cycling performance [41,42] and even dendrite suppression [41]. However, to keep the electrodes intact, past studies on OIPC-containing electrodes still required binders, which are polysaccharides for graphite [36,38,39], silicon [34,36], and silicon dioxide [39]; PVDF [36], poly(3,4-ethylene dioxythiophene) (PEDOT)–polystyrene sulfonate [35,37], and PEDOT–poly(diallyldimethylammonium) bis(trifluoromethylsulfonyl)imide [35] for

LiFePO₄ (LFP); PVDF for LiMn₂O₄ [36]; and graphene for transition metal salts [33,36], and additional functionality of OIPC electrolytes as binders in electrodes has yet to be explored in detail. The use of OIPC electrolytes as binders seems possible because the mechanical properties of OIPCs depend on their constituent ions, and some pure OIPCs are reportedly sticky, including the ones with bis(fluorosulfonyl)imide ([FSI]⁻) anions [43,44].

In this context, our present study took advantage of the ion-conduction and mechanical properties of OIPC–lithium salt mixtures comprising *N*-ethyl-*N*-methylpyrrolidinium ($[C_2mpyr]^+$) cations and [FSI]⁻ anions (hereafter referred to as $Li_x[C_2mpyr]_{1-x}[FSI]$), and substituted the commercial polymer binder with them to offer novel polymer-binder-free electrodes for advanced LIBs. The addition of the lithium salt to this OIPC was carried out to make the composites Li⁺ conductors as well as provide a Li⁺ source for electrochemical reactions at both electrodes. The lithium salts with identical anions as the OIPC are typically selected for simplicity, where the binary mixture has three constituents: OIPC cations, OIPC anions, and Li⁺ ions; in this case, Li⁺ ions are regarded as a replacement for OIPC cations in the 3D lattice [26]. LFP was chosen as a cathode active material because of its excellent cyclability [45] and safety (e.g., comparatively low sensitivity against an internal short circuit) [46]. The purposes of this study are to clarify (i) the processability, homogeneity, and mechanical intactness of LFP– $Li_x[C_2mpyr]_{1-x}[FSI]$ electrodes, especially if the polymer-binder-free approach can provide the resulting LFP cathode with an electrode loading equivalent to or even higher than the counterpart with a PVDF binder, and (ii) the electrochemical performance of these novel composite cathodes in actual rechargeable batteries. Specifically, we explored the effect of electrode formulations on the electrode fabrication process, whose variables include Li⁺ concentrations in $Li_x[C_2mpyr]_{1-x}[FSI]$ (i.e., 1, 10, and 50 mol%) and weight ratios of new ion-conductive binders ($Li_x[C_2mpyr]_{1-x}[FSI]$) in the electrode layer (i.e., 15, 30, and 50 wt%). It is known that, at room temperature, the physical state of $Li_x[C_2mpyr]_{1-x}[FSI]$ changes from solid (i.e., OIPC) to solid + liquid (≤ 10 mol%) to liquid (i.e., an IL at 50 mol%) with a Li⁺-concentration increase [31,34]; therefore, the selected Li⁺ concentrations provide insights into how the physical state of the ion-conductive binder impacts the processability of polymer-binder-free slurries and electrodes. Some LFP– $Li_x[C_2mpyr]_{1-x}[FSI]$ cathodes were employed for cell evaluation in a lithium-metal-battery (LMB) configuration. Finally, the polymer-binder-free LFP– $Li_x[C_2mpyr]_{1-x}[FSI]$ cathode was placed in the condition where an excessive Li⁺ source (i.e., lithium-metal anode) is not available (i.e., paired with a graphite– $Li_{0.10}[C_2mpyr]_{0.90}[FSI]$ anode), and preliminary demonstration of its full-cell operation progresses the realization of safe OIPC-based rechargeable batteries based on intercalation chemistry.

2. Materials and Methods

2.1. Cathode Formulation

2.1.1. Polymer-Binder-Containing Cathode Formulation

For the preparation of a cathode with a polymer binder, the active material was LFP (M121, Aleees, Taoyuan, Taiwan), the electron-conductive additive was carbon black (C-nergy Super C65, Imerys Graphite & Carbon, Bodio, Switzerland), the binder was PVDF (Solef 5130, Solvay, Brussels, Belgium), and the solvent was *N*-methyl-2-pyrrolidone (NMP, 99%, Sigma-Aldrich, St. Louis, MO, USA). First, the PVDF binder was dissolved in NMP to formulate a 10 wt% solution, which facilitates homogenization of an electrode slurry later. In atmospheric conditions, 84 wt% of LFP, 10 wt% of carbon black, and 6 wt% of PVDF were mixed with NMP using a spatula. After that, all the compounds were mixed with three $\phi 5$ mm zirconia balls using a planetary ball mill (PM 100, Retsch, Haan, Germany) for 48 min (i.e., 8 cycles of five-minute mixing and one-minute rest, where the mixing direction

was reversed every cycle) at 300 rpm. The solvent was added until the viscosity of the slurry became coatable (the final solid-content ratio of the slurry was 35%). In a laboratory, the doctor blade film coater (TMAX-TMH, Xiamen Tmax Battery Equipments Limited, Xiamen, China) coated the mixed slurry on aluminum (15 μm thickness) or carbon-coated aluminum (18 μm total thickness with 1.5 μm carbon thickness per side) sheets with three different wet gaps: 100, 500, and 1000 μm . The coated sheets were dried at 50 $^{\circ}\text{C}$ for >12 h in an ambient condition and transferred to an Ar-filled glove box (with $\text{O}_2 < 10 \text{ ppm}$ and $\text{H}_2\text{O} < 0.1 \text{ ppm}$) for storage. Test electrodes for coin-cell experiments were made by punching the coated sheets into $\varnothing 14 \text{ mm}$ disks and pressing using a pellet die ($\varnothing 16 \text{ mm}$) at room temperature under 0.5 MPa of pressure (which was conducted outside the glove box). The electrode disks were also dried in a vacuum at 50 $^{\circ}\text{C}$ for >12 h before cell assembly in the glove box.

2.1.2. Polymer-Binder-Free Cathode Formulation

The preparation of polymer-binder-free slurry followed a similar procedure for polymer-binder-containing cathodes (Section 2.1.1). The active material, conductive additive, and solvent were the same, but this time, the binder was a binary mixture of $[\text{C}_2\text{mpyr}][\text{FSI}]$ (>99%, Boron Molecular, Noble Park, Australia) and LiFSI (IONEL™ LF-101, Nippon Shokubai, Osaka, Japan). The procedure started with drying $[\text{C}_2\text{mpyr}][\text{FSI}]$ in a vacuum at 50 $^{\circ}\text{C}$ for >12 h. Both $[\text{C}_2\text{mpyr}][\text{FSI}]$ and LiFSI were weighed in the glove box. The OIPC-containing slurry was prepared based on the “*all-in-one*” method [34,38], where all ingredients are added at once for mixing, but the obvious difference from the previous studies using water-based slurries is that no secondary solvents are needed because both $[\text{C}_2\text{mpyr}][\text{FSI}]$ and LiFSI dissolve in NMP well. In atmospheric conditions, $[\text{C}_2\text{mpyr}][\text{FSI}]$ and LiFSI were mixed with LFP and carbon black in NMP. A homogeneous slurry was obtained by mixing it in the ball mill. Additional NMP was added until the viscosity of the slurry became coatable after mixing by hand using a spatula (the final solid-content ratio was between 35 and 60 wt%). The subsequent steps were also the same as those described in Section 2.1.1. The weight percentages of LFP and carbon black were fixed at 90:10 wt%, and their individual weight ratios in the final $\text{LFP}-\text{Li}_x[\text{C}_2\text{mpyr}]_{1-x}[\text{FSI}]$ electrodes were dependent on the fraction of $\text{Li}_x[\text{C}_2\text{mpyr}]_{1-x}[\text{FSI}]$. Table 1 summarizes the electrode formulations of the $\text{LFP}-\text{Li}_x[\text{C}_2\text{mpyr}]_{1-x}[\text{FSI}]$ electrodes made in this study.

Table 1. Electrode formulations of the polymer-binder-free $\text{LFP}-\text{Li}_x[\text{C}_2\text{mpyr}]_{1-x}[\text{FSI}]$ electrodes and polymer-binder-containing LFP electrode.

Label	LFP + Carbon Black: $\text{Li}_x[\text{C}_2\text{mpyr}]_{1-x}$ [FSI] [wt%]	$[\text{C}_2\text{mpyr}]^+:\text{Li}^+$ [mol%]	Weight Ratio [wt%]				
			LFP (M121)	Carbon Black (Super C65)	$[\text{C}_2\text{mpyr}]$ [FSI]	LiFSI (LF-101)	PVDF (Solef 5130)
LFP-15w-Li0.01	85:15	99:1	77.27	8.61	14.02	0.09	0
LFP-15w-Li0.10	85:15	90:10	77.38	8.61	13.11	0.90	0
LFP-15w-Li0.50	85:15	50:50	77.28	8.59	8.64	5.49	0
LFP-30w-Li0.10	70:30	90:10	62.48	7.51	28.02	1.99	0
LFP-30w-Li0.50	70:30	50:50	62.48	7.50	18.36	11.66	0
LFP-50w-Li0.01	50:50	99:1	44.64	5.36	49.68	0.32	0
LFP-50w-Li0.10	50:50	90:10	44.63	5.36	46.70	3.31	0
LFP-50w-Li0.50	50:50	50:50	44.61	5.36	30.61	19.42	0
LFP-6w-PVDF (Ref.)	100:0	N/A	84.04	9.88	0	0	6.08

2.2. Thermal Analysis

The thermal behavior of $\text{LFP}-\text{Li}_x[\text{C}_2\text{mpyr}]_{1-x}[\text{FSI}]$ was investigated by differential scanning calorimetry (DSC) using a 214 Polyma instrument (Netzsch, Selb, Germany). For the detailed procedure, please see Section S3 in Supporting Information.

2.3. Scanning Electron Microscopy and Energy-Dispersive X-Ray

Some electrodes were structurally analyzed before cycling via scanning electronic microscopy (SEM) using a JSM IT 300 series microscope (JEOL, Tokyo, Japan). Energy dispersive X-ray (EDX) experiments were performed in the same machine by an Oxford X-Max 50 mm² EDX detector. The samples for cross-sectional observations were prepared by the procedure described previously [38]. Samples were placed on the stage of an air-sensitive holder in the glove box and transferred to the antechamber of the microscope. This ensures that all the images were unaffected by the ambient conditions (e.g., moisture).

2.4. Battery Tests

2.4.1. Coin Cell Assembly

Experiments were performed in coin cells using a CR2032 format. The electrolyte was an IL with the same constituent ions as the ion-conductive binder, i.e., Li_{0.50}[C₂mpyr]_{0.50}[FSI]. Coin cells were assembled in the glove box and followed the stacking order from the bottom to the top: a negative case, a 1 mm spacer, an anode (either a lithium metal disk or preconditioned graphite–Li_{0.10}[C₂mpyr]_{0.90}[FSI] anode disk), a separator (Celgard 3501 in ø19 mm, Celgard, Charlotte, NC, USA) filled with 100 µL of Li_{0.50}[C₂mpyr]_{0.50}[FSI], a testing cathode, a 0.5 mm spacer, a spring, and a positive case with a gasket.

For the LMB configuration, both sides of the lithium foil (thickness of 50 µm, Ganfeng Lithium, Xinyu, China) were brushed, followed by punching into disks (diameter of 16 mm).

For experiments in a full-cell setup, a previously studied graphite–Li_{0.10}[C₂mpyr]_{0.90}[FSI] anode comprising 63.0 wt% of graphite, 3.50 wt% of carbon black (Super C65), 3.50 wt% of Na-CMC (average molecular weight: 70,000 g/mol, Sigma-Aldrich, St. Louis, MO, USA), and 30.0 wt% of Li_{0.10}[C₂mpyr]_{0.90}[FSI] was used [38]. This electrode was preconditioned in a solid-state half-cell comprising Li | electrospun PVDF–Li_{0.10}[C₂mpyr]_{0.90}[FSI] solid-electrolyte membrane | graphite–Li_{0.10}[C₂mpyr]_{0.90}[FSI] anode at 0.1C, 50 °C for three cycles [38]. After the formation of an SEI on graphite through this procedure, the preconditioned graphite–Li_{0.10}[C₂mpyr]_{0.90}[FSI] anode was taken from the disassembled cell in the glove box and used for full-cell assembly.

2.4.2. Electrochemical Tests

The galvanostatic charge and discharge were carried out using the Neware battery cycler at 50 °C. The first step was a 10 h rest at the open circuit voltage (OCV). After that, the constant current–constant voltage (CCCV) mode was applied with a current rate of 0.1C, with 10 min of resting time between charging and discharging. The maximum capacities of the cathodes were calculated considering 150 mAh/g as the nominal capacity for the LFP. Then, this nominal value was multiplied by the active material mass present on the cathode, resulting in the considered 1C capacity. The cut-off voltages were 2.5 and 4.2 V. Three preliminary cycling experiments were performed. When these three cycles showed expected behaviors as described in the literature for LFP (i.e., low polarization, the plateau at ≈3.4 V, and the discharge capacity of ≈150 mAh/g) [47], the cathode was further charged and discharged for 10 more cycles. The test parameters for this further aging experiment were the same as the first three cycles, but the 1C nominal capacity was updated to the experimental one, i.e., the capacity obtained in the third discharge step was considered as the cell capacity. After a total of 13 cycles, the rate capability experiments were performed with the sequence: 0.1C (reference value) → 0.2C → 0.5C → 1C → 2C. To evaluate charge and discharge rate capabilities separately, either the charge or discharge rate was changed, and the other rate was kept constant (i.e., 0.1C). After the rate tests, long-term

cycling (80 cycles) tests were conducted, which followed the same test parameters as the 10 extra cycles.

3. Results

3.1. Effect of the $\text{Li}_x[\text{C}_2\text{mpyr}]_{1-x}[\text{FSI}]$ Content and Li^+ Concentration on the Nominal Areal Capacity and Electrode Density of the Composite Electrode

The polymer-binder-free slurry was prepared in the “all-in-one” method [34], as illustrated in Figure 1a. The effect of the two different types of proportions was evaluated, which included the quantity of $\text{Li}_x[\text{C}_2\text{mpyr}]_{1-x}[\text{FSI}]$ in the electrode (depicted in Figure 1a as Variable Proportion 1 in x_1 wt%) and the quantity of Li^+ ions in $\text{Li}_x[\text{C}_2\text{mpyr}]_{1-x}[\text{FSI}]$ (referred to as Variable Proportion 2 in x_2 mol%). For clarity, Variable Proportion 1 was referred to as the “ $\text{Li}_x[\text{C}_2\text{mpyr}]_{1-x}[\text{FSI}]$ content”, and Variable Proportion 2 was referred to as the “ Li^+ concentration”, even though the weight ratio of Li^+ ions in the composite electrode varied along with both evaluated proportions (as indicated in Table 1). Analyzing the influence of $\text{Li}_x[\text{C}_2\text{mpyr}]_{1-x}[\text{FSI}]$ content is crucial because it directly affects the binding properties of electrode ingredients. On the other hand, the Li^+ concentration is important because it influences the ionic conductivity and phase behavior of $\text{Li}_x[\text{C}_2\text{mpyr}]_{1-x}[\text{FSI}]$ [31].

As shown in Figure 1b, LFP–6w-PVDF slurry was successfully coated at a thickness of 100 μm without any cracking after drying. At 500 μm , the dried electrode showed small cracks throughout the entire coated layer, and at 1000 μm , the cracks were more significant, and the underlying aluminum substrate was clearly visible in the cracked regions. The dried electrodes with these coating thicknesses (i.e., 500 and 1000 μm) detached completely from the current collector when placed in a vertical position. In contrast, the dried polymer-binder-free LFP–50w-Li0.01 remained intact for all three evaluated wet gaps. Although the surface roughness tended to increase with an increase in the wet gap, the dried LFP–50w-Li0.01 had no cracks (Figure 1c). This confirms that $\text{Li}_x[\text{C}_2\text{mpyr}]_{1-x}[\text{FSI}]$ can act as a binder to hold electrode ingredients together in a certain shape, and, at some conditions, $\text{Li}_x[\text{C}_2\text{mpyr}]_{1-x}[\text{FSI}]$ can support higher electrode loading than PVDF without obvious mechanical failures of the electrode. A detailed perspective on the competitiveness of this polymer-binder-free approach with the conventional electrode preparation using PVDF is provided in Section S1 (Table S1) in Supporting Information.

The effect of the two variables on the nominal areal capacity of the LFP– $\text{Li}_x[\text{C}_2\text{mpyr}]_{1-x}[\text{FSI}]$ electrode was evaluated (Figure 1d). Indeed, some compositions enabled coating at a 1000 μm gap without a cracking issue after drying. The compositions resulting in unbroken thick electrodes are presented as the red region in Figure 1d. This region corresponds to the highest $\text{Li}_x[\text{C}_2\text{mpyr}]_{1-x}[\text{FSI}]$ content (i.e., 50 wt%). The color bar on the right side in Figure 1d displays values of the nominal areal capacity, and each data point was obtained by the average of four electrodes of the same experiment. Considering the electrode loading and the specific capacity of LFP (i.e., 150 mAh/g), it is possible to achieve a thick LFP– $\text{Li}_x[\text{C}_2\text{mpyr}]_{1-x}[\text{FSI}]$ electrode using 50 wt% $\text{Li}_x[\text{C}_2\text{mpyr}]_{1-x}[\text{FSI}]$ with a nominal areal capacity of as high as 3.74 mAh/cm² (at 50 mol% Li^+). While only the highest $\text{Li}_x[\text{C}_2\text{mpyr}]_{1-x}[\text{FSI}]$ content supported a high areal capacity (using a coating gap of 1000 μm), all the LFP– $\text{Li}_x[\text{C}_2\text{mpyr}]_{1-x}[\text{FSI}]$ slurries were able to achieve an undamaged coating with a 100 μm wet gap, corresponding to a low nominal areal capacity in the color bar (i.e., green region). This result highlights the binding ability of $\text{Li}_x[\text{C}_2\text{mpyr}]_{1-x}[\text{FSI}]$; it can function as a binder even at a relatively low weight ratio (i.e., 15 wt%). When comparing the LFP loading values of the electrodes prepared by the same wet gap (i.e., 100 μm) at the fixed Li^+ concentration (i.e., 1 mol%), the electrode with 50 wt% $\text{Li}_{0.01}[\text{C}_2\text{mpyr}]_{0.99}[\text{FSI}]$ (LFP–50w-Li0.01) had an LFP loading of 2.17 mg/cm², whereas it was measured to be 1.41 mg/cm² for 15 wt% $\text{Li}_{0.01}[\text{C}_2\text{mpyr}]_{0.99}[\text{FSI}]$ (LFP–15w-Li0.01). The LFP loading values

of both LFP–Li_{0.01}[C₂mpyr]_{0.99}[FSI] electrodes were different from that of LFP–6w-PVDF (which had an LFP loading of 1.71 mg/cm²). This difference in LFP loading, observed across all electrodes obtained using the same wet gap, is caused by the varying solid ratios in the different Li_x[C₂mpyr]_{1-x}[FSI] contents tested. For instance, in the LFP-50w-Li0.01, less NMP was needed, resulting in a solid ratio of 60.1 wt%. Conversely, the LFP-15w-Li0.01 slurry resulted in a solid ratio of 37.4 wt%.

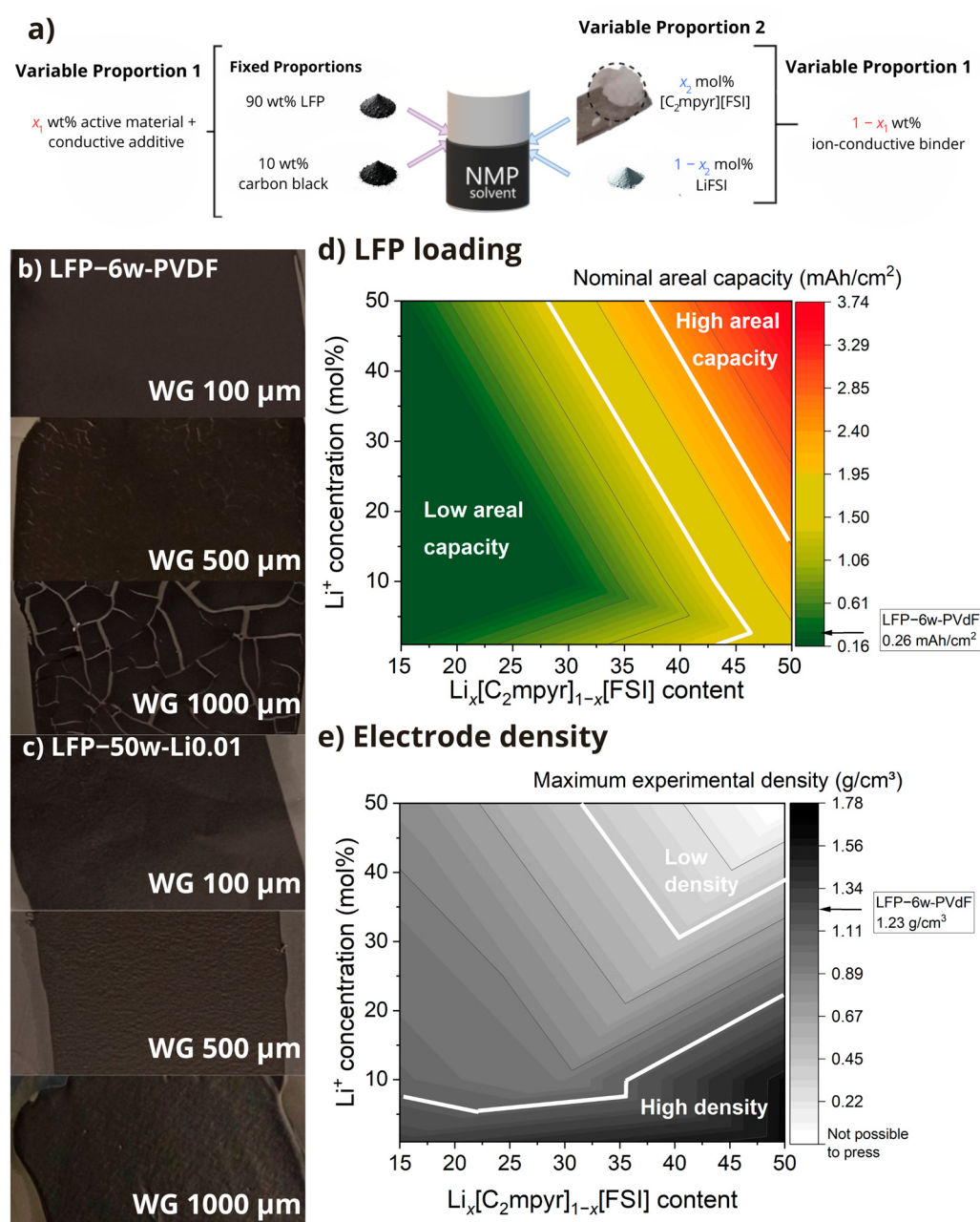


Figure 1. (a) The formulation of a polymer-binder-free LFP–Li_x[C₂mpyr]_{1-x}[FSI] slurry with the two variable proportions. (b,c) The photos of the dried surfaces of (b) polymer-binder-containing (LFP–6w-PVDF) and (c) polymer-binder-free (LFP–50w-Li0.01) electrodes on Al prepared using different wet gaps. (d,e) Contour graphs for (d) the calculated nominal areal capacity and (e) the experimentally measured electrode density of polymer-binder-free LFP–Li_x[C₂mpyr]_{1-x}[FSI] electrodes on Al.

The LFP–Li_x[C₂mpyr]_{1-x}[FSI] electrodes were also evaluated in terms of the experimentally achievable electrode density, as shown in Figure 1e. The electrode sheet of each studied formulation (with a coating gap of 100 μm) was punched into ø14 mm disks and

compressed using a pellet die to produce the densified electrode. The electrodes with the highest content of $\text{Li}_x[\text{C}_2\text{mpyr}]_{1-x}[\text{FSI}]$ and Li^+ ions (i.e., LFP–50w-Li0.50) formed a soft film that was easily deformed and impossible to withstand the compression process. SEM experiments (Figure S1) show that the electrode surface of this formulation (LFP–50w-Li0.50) had a higher surface roughness than others, and particles tended to form big chunks with wavy edges (which would visually prove that $\text{Li}_{0.50}[\text{C}_2\text{mpyr}]_{0.50}[\text{FSI}]$ stays as an amorphous phase in the composite electrode). These obvious differences are a result of a higher amount of $\text{Li}_x[\text{C}_2\text{mpyr}]_{1-x}[\text{FSI}]$ and its Li^+ concentration, providing the electrode with a greater volume of the amorphous phase (that is easily deformed by external pressure) than others [48]. Indeed, $\text{Li}_x[\text{C}_2\text{mpyr}]_{1-x}[\text{FSI}]$ becomes soft as the Li^+ concentration increases [34], which reduces the structural rigidity of the LFP– $\text{Li}_x[\text{C}_2\text{mpyr}]_{1-x}[\text{FSI}]$ electrode. This hypothesis has also been supported by the thermal behavior of LFP–50w-Lix ($x = 0.01, 0.10$, or 0.50) in Table 2 and Figure S2; $\text{Li}_{0.01}[\text{C}_2\text{mpyr}]_{0.99}[\text{FSI}]$ in the LFP electrode is identified as solid with an enhanced disorder, whereas both $\text{Li}_{0.10}[\text{C}_2\text{mpyr}]_{0.90}[\text{FSI}]$ and $\text{Li}_{0.50}[\text{C}_2\text{mpyr}]_{0.50}[\text{FSI}]$ in the electrode appear to be amorphous, showing the crystallization peak at around 219 ± 5 °C, similarly reported for annealed $\text{Li}_{0.50}[\text{C}_2\text{mpyr}]_{0.50}[\text{FSI}]$ [31]. Therefore, to balance the achievable areal capacity and the processability of the LFP– $\text{Li}_x[\text{C}_2\text{mpyr}]_{1-x}[\text{FSI}]$ electrode, reducing the Li^+ concentration is necessary at 50 wt% $\text{Li}_x[\text{C}_2\text{mpyr}]_{1-x}[\text{FSI}]$. Alternatively, reducing the $\text{Li}_{0.50}[\text{C}_2\text{mpyr}]_{0.50}[\text{FSI}]$ content also provides enough rigidity for the composite electrode to be compressed because of the reduced weight fraction of the softer material (than LFP and carbon black particles) in the electrode.

Table 2. Glass transition temperature (T_g), crystallization temperature (T_c), melting point (mp.), and entropy of fusion (ΔS) of the samples estimated from the heating trace of DSC.

Sample	Scan	T_g [°C]	T_c [°C]	mp. [°C]	ΔS [J K ⁻¹ mol ⁻¹]	Ref.
LFP–50w-Li0.01	1st	N/D	N/D	204	4.8	This work
LFP–50w-Li0.01	2nd	N/D	N/D	205	3.7	This work
LFP–50w-Li0.10	1st	N/D	224	160	1.4	This work
LFP–50w-Li0.10	2nd	N/D	N/D	205	4.6	This work
LFP–50w-Li0.50	1st	N/D ^a	214	N/D	N/D	This work
LFP–50w-Li0.50	2nd	−71.5	N/D	N/D	N/D	This work
[C ₂ mpyr][FSI]	2nd	N/D	N/D	203	9.6	[26]
$\text{Li}_{0.01}[\text{C}_2\text{mpyr}]_{0.99}[\text{FSI}]$	2nd	N/D	N/D	193	6.4	[26]
$\text{Li}_{0.10}[\text{C}_2\text{mpyr}]_{0.90}[\text{FSI}]$	2nd	N/D	N/D	156	1.9	[26]
$\text{Li}_{0.50}[\text{C}_2\text{mpyr}]_{0.50}[\text{FSI}]$	2nd	−81	N/D ^b	N/D	N/D	[31]

N/D: Not detected. ^a Not measured as the heating trace started from 30 °C. ^b In the 1st heating trace, $T_c = 124$ and 196 °C for non-annealed and annealed samples, respectively.

From Figure 1e, the three corners of the two variable proportions (except for the top right corner; i.e., LFP–50w-Li0.01, LFP–15w-Li0.01, and LFP–15w-Li0.50) are worth investigating further. As LFP–50w-Li0.01 was able to provide both high nominal areal capacity and high electrode density, this composite electrode was evaluated to see if it could truly show a high areal capacity of >1.5 mAh cm^{−2} (Section 3.3.1). On the other hand, both LFP–15w-Li0.01 and LFP–15w-Li0.50 were suitable to generate compressible electrodes with a coating gap of 100 µm even though the amount of $\text{Li}_x[\text{C}_2\text{mpyr}]_{1-x}[\text{FSI}]$ was relatively low. For them, half-cell tests were performed to evaluate the effect of the Li^+ concentration on their electrochemical performance, especially aiming to gain superior charge/discharge rate capabilities (Section 3.3.2).

3.2. Homogeneity and Solubility of the Polymer-Binder-Free LFP– $\text{Li}_x[\text{C}_2\text{mpyr}]_{1-x}[\text{FSI}]$ Electrode

In the electrode layer, the uniform distribution of electrode ingredients (especially for electron- and ion-conductive materials) is important to maximize the electrochem-

ical performance of the electrode [34]. Therefore, the dispersibility of the ingredients in the LFP–Li_x[C₂mpyr]_{1-x}[FSI] electrode was evaluated before the cell-cycling tests. LFP–50w-Li0.01 with the highest nominal areal capacity was chosen for the analysis by means of surface and cross-section SEM, whose results are presented in Figures 2a and 2b, respectively. The surface image appears to be flat and sufficiently uniform without any localized materials (e.g., OIPC electrolyte grains that would form during drying an electrode slurry [38]). The image also has relatively dark regions with blurred particle edges. These indicate that 50 wt% Li_{0.01}[C₂mpyr]_{0.99}[FSI] helped the deformation of the electrode while under compression and filled the pores to connect particles. The cross-sectional image shows almost the same appearance as the surface image. Although the image contains some artifacts generated by cutting the electrode (e.g., diagonal lines that run at ca. 30° from the line of the current collector surface and a particle attached to the cross-sectional surface), the densification of the electrode layer towards the current collector is clearly seen; no pores are observed at the bottom region of the electrode. This further highlights the excellent deformability of Li_{0.01}[C₂mpyr]_{0.99}[FSI] against external pressure. These images strengthen the idea that the complete replacement of a liquid electrolyte solution in the pores of the LIB electrode (i.e., exclusion of unfilled pores) might be possible by employing a sufficient amount of Li_x[C₂mpyr]_{1-x}[FSI] as an ion-conductive binder. If the amount of Li_x[C₂mpyr]_{1-x}[FSI] is relatively small (i.e., ≤30 wt%), some pores in the electrode likely remain unfilled, but such conditions still can provide effective ion conduction pathways (that presumably expand along with the particle surfaces) throughout the electrode layer (especially if they are percolated) [34,38].

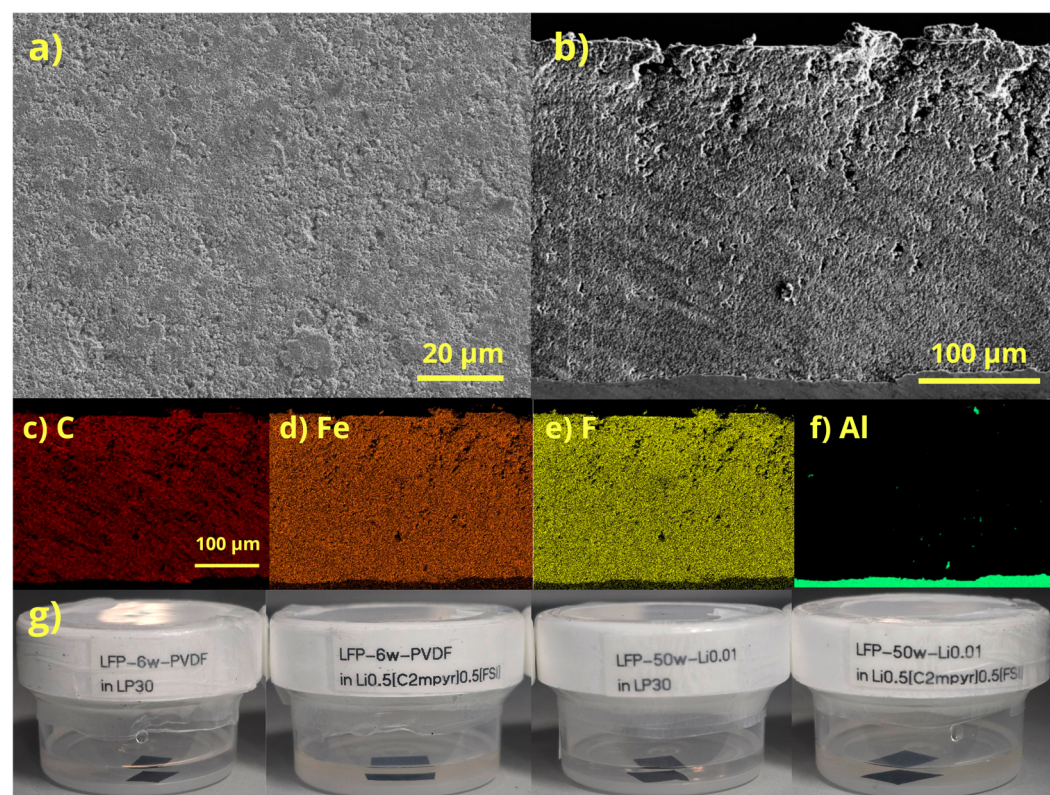


Figure 2. (a) Surface and (b) cross-sectional SEM images of LFP–50w-Li0.01 on Al current collector. EDX elemental mappings of (c) C, (d) Fe, (e) F, and (f) Al, for the area resolved in (b). (g) Pictures of LFP–6w–PVDF (first and second samples, from left to right) and LFP–50w–Li0.01 (third and fourth samples) pieces in LP30 and Li_{0.50}[C₂mpyr]_{0.50}[FSI] after being stored in an oven at 50 °C for >16 h with the outside dew point of <-40 °C (at room temperature).

To provide insights into the electrode ingredients' dispersibility further, EDX was performed for the same cross-section as Figure 2b. The excellent dispersibility was proven by elemental mapping, showing that carbon (Figure 2c, mainly contributed by carbon black and $[C_2mpyr]^+$), iron (Figure 2d, originating from LFP), and fluorine (Figure 2e, sourced from $[FSI]^-$) are well distributed within the electrode layer. No localized electrode ingredients are resolved. The result clarifies that the “*all-in-one*” method using NMP can provide the electrode layer with a better distribution of the ingredients than that using water and a secondary solvent [34,38]. This is likely to be due to the high solubility of $Li_x[C_2mpyr]_{1-x}[FSI]$ in NMP and the use of only one solvent, both of which tend to restrict the isolation of $Li_x[C_2mpyr]_{1-x}[FSI]$ from particle surfaces while evaporating NMP. Some pieces of aluminum were detected on the surface of the cross-section (Figure 2f), which confirmed the presence of artifacts stemming from the electrode cutting process, but they did not affect the evaluation of the dispersibility of the electrode ingredients.

Additionally, to check the stability of the coated layer, some solubility tests were conducted at 50 °C. The solubilities of both polymer-binder-containing (LFP–6w-PVDF) and polymer-binder-free (LFP–50w-Li0.01) electrodes in a commercial electrolyte solution (i.e., LP30, which is 1 M $LiPF_6$ in ethylene carbonate (EC)–dimethyl carbonate (DMC), 50:50 vol%) and IL (i.e., $Li_{0.50}[C_2mpyr]_{0.50}[FSI]$ which comprises the same ionic constituents as the ion-conductive binder in the electrode) were compared. LFP–6w-PVDF remained intact in both liquids, as indicated by the achromatic color of the liquids (Figure 2g). Similarly, LFP–50w-Li0.01 did not break apart in both liquids; LFP–50w-Li0.01 was stable for at least 2 weeks. To avoid using different anions in the cathode (i.e., $[FSI]^-$) and separator layers (i.e., PF_6^-), the subsequent battery tests for LFP– $Li_x[C_2mpyr]_{1-x}[FSI]$ electrodes were conducted with a polyolefin separator + $Li_{0.50}[C_2mpyr]_{0.50}[FSI]$.

3.3. Cell Performances of Polymer-Binder-Free LFP– $Li_x[C_2mpyr]_{1-x}[FSI]$ Electrodes

3.3.1. Thick Composite Electrodes for High Areal Capacity

LFP–50w-Li0.01 with a high nominal areal capacity (LFP loading: 11.7 mg/cm²) was used for battery evaluation in an LMB configuration (with an interlayer filled with $Li_{0.50}[C_2mpyr]_{0.50}[FSI]$). Its cell test showed the expected charge/discharge profile of LFP, i.e., intercalation/deintercalation processes at around 3.4 V vs. Li/Li⁺ [47], as seen in Figure 3a by the characteristic two-phase plateau of Fe^{2+} and Fe^{3+} in the LFP crystal. However, its discharge capacity was lower than the theoretical value of LFP (170 mAh/g) [49,50]: 135.7 mAh/g for the first cycle and 128.9 mAh/g for the 13th cycle. The same LFP was tested for the regular formulation with PVDF (i.e., LFP–6w-PVDF) in LP30 and showed a discharge capacity of 155.9 mAh/g (Figure S3). This confirms that the maximum achievable capacity of this LFP is <170 mAh/g, which is because this material is carbon-coated for conductivity improvement (indeed, the supplier certifies its capacity as ≥150 mAh/g). In addition, LFP–6w-PVDF in $Li_{0.50}[C_2mpyr]_{0.50}[FSI]$ was tested, resulting in an additional loss of 9 mAh/g of the discharge capacity (Figure S3). This means that even if the commercial polymer-binder formulation is employed, only 146.9 mAh/g can be obtained for our setup.

The charge and discharge profiles of LFP–50w-Li0.01 present a high overvoltage, e.g., a voltage difference between the charge and discharge plateaus of >0.1 V. This was probably caused by a thick layer of this electrode, which increases diffusion polarization within the electrode layer and increases resistance [51]. To clearly evaluate the overvoltage, a dQ/dV analysis was conducted. A pair of sharp dQ/dV peaks appears with a peak height of 3.0 ± 0.5 Ah/gV (Figure 3b). The differences between peak voltages were estimated to be 0.12 V for the first cycle, 0.13 V for the fifth cycle, and 0.16 V for the 13th cycle, which became wider as the cycle number increased. This suggests that the cell resistance gradually increases over cycling, which is likely to be due to the rearrangement of LFP

and carbon black particles induced by the volume change in the active materials during cycling. This would cause the gradual disconnection of LFP particles from the electrode's conductive pathways. Both contribute to a decrease in the observable capacity as the cycle test progresses.

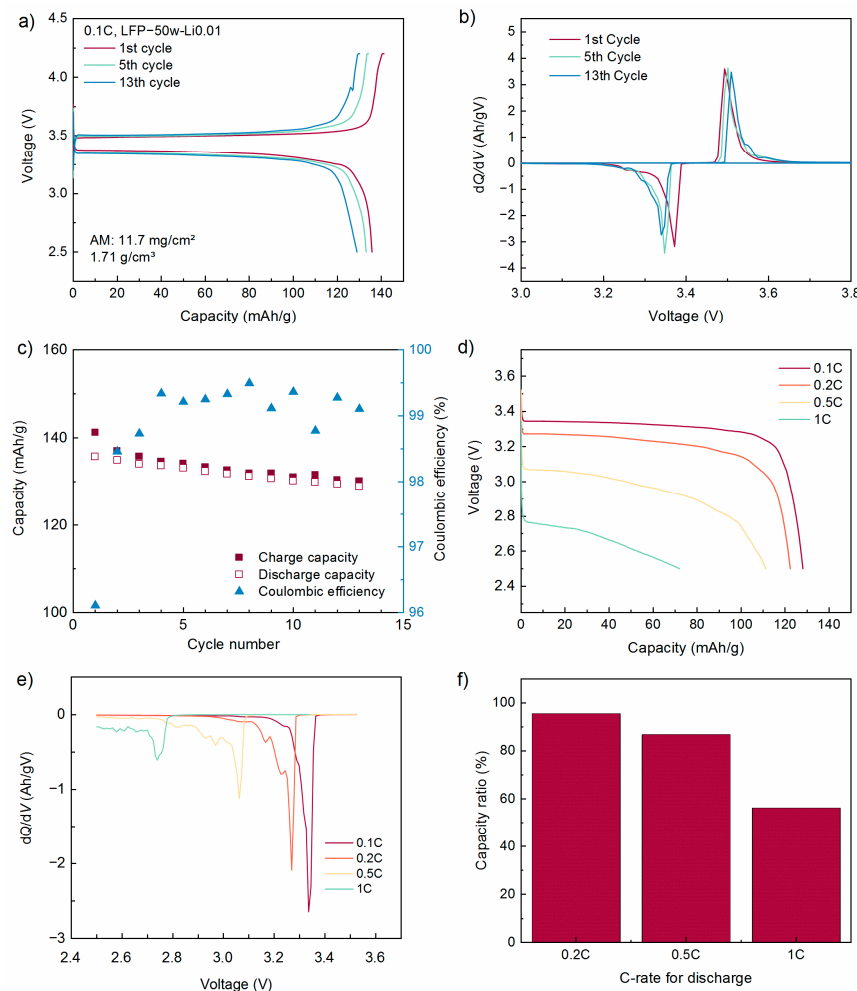


Figure 3. The results of the battery tests for the thick polymer-binder-free LFP–Li_{0.01}[C₂mpyr]_{0.99}[FSI] cathode (LFP–50w-Li0.01) on Al paired with Li metal in Li_{0.50}[C₂mpyr]_{0.50}[FSI] at 50 °C. (a) The charge/discharge profiles of LFP–50w-Li0.01 at 0.1C at the selected cycles. (b) The dQ/dV profiles of LFP–50w-Li0.01 at 0.1C at the selected cycles. (c) The charge/discharge capacities and Coulombic efficiency of LFP–50w-Li0.01 for 13 cycles at 0.1C. (d) The voltage profiles of LFP–50w-Li0.01 during the discharge step under different C-rates from 0.1C to 1C. (e) The dQ/dV profiles of LFP–50w-Li0.01 during discharging at different C-rates. (f) The discharge capacity ratios of LFP–50w-Li0.01 for different C-rates (where the discharge capacity at 0.1C was set as 100%).

Indeed, the charge/discharge capacities of LFP–50w-Li0.01 in Li_{0.50}[C₂mpyr]_{0.50}[FSI] decreased over cycling (Figure 3c); the capacity loss during cycling was estimated to be 1.9% from the first to the fifth cycles and 3.2% from the fifth to the 13th cycle. Conversely, the capacity loss for LFP–6w-PVDF in Li_{0.50}[C₂mpyr]_{0.50}[FSI] was negligible from the first to the fifth cycles and 0.7% from the fifth to the 13th cycles (Figure S4a), which is considerably lower than LFP–50w-Li0.01. This implies that the binding ability of Li_x[C₂mpyr]_{1-x}[FSI] to hold the electrode structure during cycling would be enough for multiple cycles, but it would not be as strong as PVDF. However, it should be noted that this deduction is from the comparison between different LFP-loading values (i.e., 11.7 mg/cm² for LFP–50w-Li0.01 vs. 1.71 mg/cm² for LFP–6w-PVDF) as well, and LFP–6w-PVDF could not reach a comparable loading value of >10 mg/cm² (i.e., a wet gap of >500 μm, as discussed in

Section 3.1). Therefore, polymer-binder-free formulations are still effective in offering cell cycling with a relatively high LFP loading that cannot be reached by conventional polymer-binder-containing formulations.

As for the Coulombic efficiency, both LFP–50w-Li0.01 and LFP–6w-PVDF in $\text{Li}_{0.50}[\text{C}_2\text{mpyr}]_{0.50}[\text{FSI}]$ showed different behavior over cycling. The Coulombic efficiency of LFP–50w-Li0.01 (in Figure 3c) gradually increased from 96.1% at the first cycle to 99.4% at the fourth cycle. After that, it fluctuated $\approx 99\%$. In contrast, the Coulombic efficiency of LFP–6w-PVDF was 94.2% at the first cycle and around 97% for the subsequent cycles (Figure S4b). Generally, a higher irreversible capacity and lower Coulombic efficiency are expected at the first cycle than subsequent cycles, which is due to the cathode electrolyte interphase (CEI) formation [52]. However, the Coulombic efficiency at the subsequent cycles should be as close to 100% as possible; otherwise, it might indicate some irreversible phenomena, e.g., the continuous CEI formation and loss of an active material over cycling. It is noteworthy that, at the 13th cycle, the Coulombic efficiency of LFP–50w-Li0.01 was ca. 2% higher than that of LFP–6w-PVDF. This implies that, although the irreversible phenomena are present in both cases, LFP–50w-Li0.01 is more stable than LFP–6w-PVDF. The result implies that the combination of $\text{Li}_{0.50}[\text{C}_2\text{mpyr}]_{0.50}[\text{FSI}]$ and PVDF contributes to a relatively large irreversible capacity (i.e., a decrease in the Coulombic efficiency), which would be related to the dehydrofluorination of PVDF reported on the anode side [38].

When LFP–50w-Li0.01 is tested at high discharge currents (Figure 3d,f), its discharge capacity at 1C decreases to 56% of that measured at 0.1C, and it cannot perform a sufficient discharge at 2C or higher. Although the previous study suggested that increasing the electrode loading potentially decreases the internal resistance of an electrode layer by an increased number of parallel connections (i.e., electron conduction pathways along the direction parallel with the current-collector surface) [51], the discharge rate capability of LFP–50w-Li0.01 implied that another increase in the resistance negated such a positive effect because of the elongated electronic and ionic pathways (along the normal to the current-collector surface) in thick electrodes. The addition of $\text{Li}_x[\text{C}_2\text{mpyr}]_{1-x}[\text{FSI}]$ to the electrode was expected to decrease ionic resistance, but it appears that the electronic resistance still limited the achievable capacity at high-current tests. Figure 3e illustrates the significant changes in the lithiation voltage of LFP (i.e., the dQ/dV peak voltage) and in its lithiation amount (i.e., the area of the dQ/dV signal) when cycled at higher currents. These changes can be caused by the dependency on the rate of Li^+ transport. In cases where there are some kinetic constraints, such as poor conductivity or slow diffusion rates, the Li^+ transport in the electrode is restricted [53]. This phenomenon would allow for the emergence of additional small peaks (following the main dQ/dV peak) that were not observed at 0.1C discharging, although another possibility of the small peaks is noise that was not sufficiently removed because of the sampling rate in this study (i.e., the instrument took a datapoint every 20-mV difference).

The results of high-rate discharge tests for LFP–50w-Li0.01 suggest this electrode is not adequate for high-power applications, but it is ideal for high-energy applications. This electrode demonstrated the actual areal capacity of 1.5–1.6 mAh/cm². A further increase in the actual areal capacity of this polymer-binder-free cathode in the LMB configuration is possible by changing the electrode composition and/or current collector. However, the half-cell experiments using the electrode with the nominal areal capacity of >2.0 mAh/cm² are challenging. A preliminary test of LFP–50w-Li0.50 coated on carbon-coated Al with the nominal areal capacity of 2.67 mAh/cm² (LFP loading: 17.86 mg/cm²) suffered from voltage fluctuations during charging (as seen in Figure S5), which might indicate micro shorts stemming from lithium dendrite formation [54]. Nevertheless, this electrode showed the first discharge capacity of 139.4 mAh/g, which was equivalent to 2.49 mAh/cm²,

demonstrating the excellent workability of the polymer-binder-free cathode for high-energy applications. Further optimization of the anode (e.g., engineering lithium-metal anode [55] and using other anode active materials that are compatible with $\text{Li}_x[\text{C}_2\text{mpyr}]_{1-x}[\text{FSI}]$ [34, 38]) and separator (e.g., ceramic coating on polyolefin separators [56–58] and the use of ceramic separators [59]) is beneficial to prevent the aforementioned micro-short issue for stable cycling of the batteries employing polymer-binder-free LFP– $\text{Li}_x[\text{C}_2\text{mpyr}]_{1-x}[\text{FSI}]$ cathodes with a high areal capacity.

3.3.2. Thin Composite Electrodes for Superior Rate Capability

The two LFP– $\text{Li}_x[\text{C}_2\text{mpyr}]_{1-x}[\text{FSI}]$ cathodes with 15 wt% $\text{Li}_x[\text{C}_2\text{mpyr}]_{1-x}[\text{FSI}]$ (i.e., LFP–15w-Li0.01 and LFP–15w-Li0.50) were selected for battery tests with limited LFP loading (i.e., the nominal areal capacity of 0.2–0.3 mAh/cm^2 , which is in the same range as LFP–6w-PVDF). In charge/discharge rate tests at 2C, two Li^+ concentrations were compared. LFP–15w-Li0.01 exhibited lower overvoltages in both charge and discharge curves than LFP–15w-Li0.50, resulting in a higher specific capacity (Figure 4a,c). The overvoltage is due to three factors: IR loss, activation polarization, and concentration polarization [60]. The immediate voltage jump caused by applying a current refers to the IR loss, and the subsequent voltage change to initiate lithiation/delithiation reactions is considered the activation polarization, while the voltage change at the end of charging/discharging reactions is related to concentration polarization. An increase in both Ohmic loss and activation polarization from LFP–15w-Li0.01 to LFP–15w-Li0.50 suggests that the electric resistance of the LFP– $\text{Li}_x[\text{C}_2\text{mpyr}]_{1-x}[\text{FSI}]$ cathode rises as the Li^+ concentration increases in its formulation. This implies that the surface area of carbon black particles covered by $\text{Li}_{0.50}[\text{C}_2\text{mpyr}]_{0.50}[\text{FSI}]$ (which is an IL) is higher than that surrounded by $\text{Li}_{0.01}[\text{C}_2\text{mpyr}]_{0.99}[\text{FSI}]$ (which is regarded as a solid composite), providing LFP–15w-Li0.50 with more tortuous electron conduction pathways than LFP–15w-Li0.01. This consideration is supported by the previous study, which reported an increased charge-transfer resistance at the Si– $\text{Li}_{0.50}[\text{C}_2\text{mpyr}]_{0.50}[\text{FSI}]$ interface when carbon black particles were preferentially covered by $\text{Li}_{0.50}[\text{C}_2\text{mpyr}]_{0.50}[\text{FSI}]$ [34]. Furthermore, a higher concentration polarization was observed for LFP–15w-Li0.50 than for LFP–15w-Li0.01. This indicates that a greater amount of Li^+ ions available within the electrode does not necessarily lead to an improvement in mass transfer. A highly Li^+ -concentrated interface is not favorable for LFP to progress its delithiation as it would lead to the formation of relatively immobile LiFSI because of the solubility limit of Li^+ in $\text{Li}_x[\text{C}_2\text{mpyr}]_{1-x}[\text{FSI}]$ at the LFP surface, resulting in a large concentration polarization [61]. As the discharge (lithiation) step comes after the charge (delithiation) step, the aforementioned issue might also affect the efficacy of LFP's delithiation.

Superior charge/discharge rate capabilities of LFP–15w-Li0.01 to LFP–15w-Li0.50 were clarified in detail as the capacity ratios at different C-rates. The capacity ratio values for both lithiation (Figure 4b) and delithiation (Figure 4d) clarify that LFP–15w-Li0.01 can offer a higher capacity than LFP–15w-Li0.50 at a high current. For instance, at a 2C current, the 0.1C capacity of LFP–15w-Li0.01 retained 97.2% for lithiation and 94.6% for delithiation, whereas LFP–15w-Li0.50 showed a capacity ratio of 81.4% for lithiation and 76.5% for delithiation. Therefore, an LFP– $\text{Li}_x[\text{C}_2\text{mpyr}]_{1-x}[\text{FSI}]$ cathode with a lower Li^+ -concentration is more useful to provide superior charge/discharge rate capabilities.

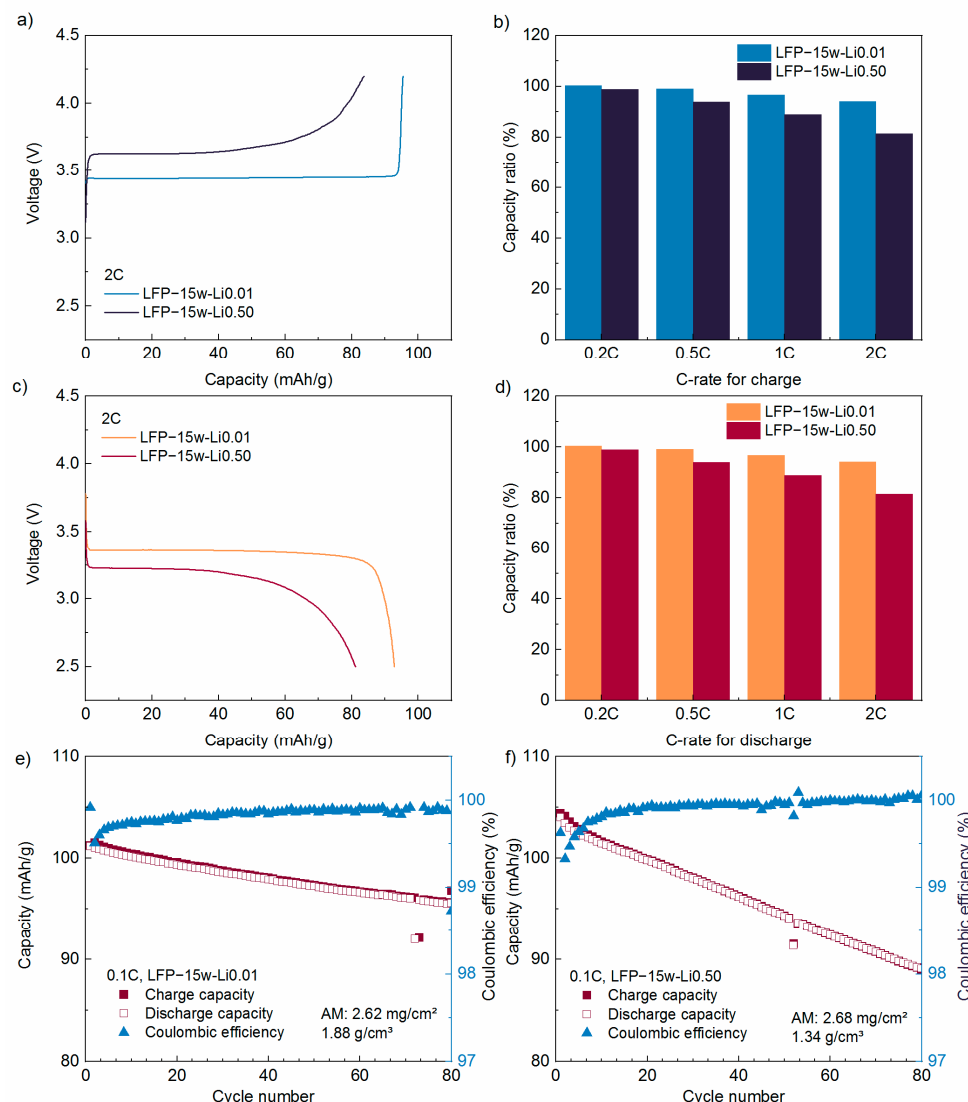


Figure 4. The results of the battery tests for thin polymer-binder-free $\text{LFP}-\text{Li}_x[\text{C}_2\text{mpyr}]_{1-x}[\text{FSI}]$ cathodes (LFP-15w-Li0.01 and LFP-15w-Li0.50) paired with Li metal in $\text{Li}_{0.50}[\text{C}_2\text{mpyr}]_{0.50}[\text{FSI}]$ at 50 °C. (a) The voltage profiles of LFP-15w-Li0.01 and LFP-15w-Li0.50 during the charge step at 2C. (b) The charge capacity ratios of LFP-15w-Li0.01 and LFP-15w-Li0.50 for different C-rates (where the charge capacity at 0.1C was set as 100%). (c) The voltage profiles of LFP-15w-Li0.01 and LFP-15w-Li0.50 during the discharge step at 2C. (d) The discharge capacity ratios of LFP-15w-Li0.01 and LFP-15w-Li0.50 for different C-rates (where the discharge capacity at 0.1C was set as 100%). (e,f) The charge/discharge capacities and Coulombic efficiencies of (e) LFP-15w-Li0.01 and (f) LFP-15w-Li0.50 for 80 cycles at 0.1C.

The cycle performances of these electrodes were also evaluated at 0.1C. Both electrodes show a continuous decrease in the capacity as the cycle number increases (Figure 4e,f). However, an obvious difference in the degradation speed was found. LFP-15w-Li0.01 experienced a loss of a ca. 6 mAh/g capacity after 80 cycles, while ca. 15 mAh/g was lost for LFP-15w-Li0.50 through the same cycling period. This result suggests that an $\text{LFP}-\text{Li}_x[\text{C}_2\text{mpyr}]_{1-x}[\text{FSI}]$ cathode with a softer $\text{Li}_x[\text{C}_2\text{mpyr}]_{1-x}[\text{FSI}]$ (e.g., LFP-15w-Li0.50 vs. LFP-15w-Li0.01) becomes more susceptible to the structural deformation of the cathode induced by the lithiation/delithiation of LFP, resulting in losing a greater amount of active LFP particles over cycling. DSC of $\text{LFP}-\text{Li}_x[\text{C}_2\text{mpyr}]_{1-x}[\text{FSI}]$ implied that the electrode layer became soft (i.e., amorphous) when the Li^+ concentration increased. Therefore, to maximize the cyclability of the $\text{LFP}-\text{Li}_x[\text{C}_2\text{mpyr}]_{1-x}[\text{FSI}]$ cathode, choosing

a low Li^+ concentration (e.g., 1 mol%) is beneficial as it offers the plastic crystalline phase of the electrolyte to hold the electrode structure. In addition, as shown in Figure S6, the discharge capacity retention of LFP–15w-Li0.01 was close to that of LFP–6w-PVDF and LFP–15w-Li0.01 showed higher Coulombic efficiency than LFP–6w-PVDF (except for the first cycle), which demonstrates a possibility for the polymer-binder-free approach in achieving the promising electrochemical performance comparable with of polymer-binder-containing LFP cathodes.

As for the change in the Coulombic efficiency over cycling, both electrodes also show different behaviors (Figure 4e,f). Although LFP–15w-Li0.01 had a higher Coulombic efficiency than LFP–15w-Li0.50 at the first few cycles, its stabilization for LFP–15w-Li0.01 takes a considerably longer cycle period than that for LFP–15w-Li0.50. A gradual increase in the Coulombic efficiency of electrodes with OIPC–lithium salt mixtures was previously referred to as “preconditioning” [34,38], whose origins have been discussed based on Joule heating as well as the restructuring of the OIPC interface, and took ca. 20 cycles to be stabilized [38]. The Coulombic efficiency of LFP–15w-Li0.50 was almost stabilized after 20 cycles, and, after that, it increased very slowly over cycling, reaching 99.99% at the 70th cycle and 100.1% at the 80th cycle, which evidences degradation processes after long cycling. In contrast, LFP–15w-Li0.01 did not show an obvious stabilization of the Coulombic efficiency after around 20 cycles; it kept increasing over cycling but still remained at a lower level (i.e., 99.8%) than that of LFP–15w-Li0.50 after 80 cycles. This difference is reasonable, as a harder ion-conductive binder (i.e., $\text{Li}_{0.01}[\text{C}_2\text{mpyr}]_{0.99}[\text{FSI}]$) is expected to take a longer period than a softer one (i.e., $\text{Li}_{0.50}[\text{C}_2\text{mpyr}]_{0.50}[\text{FSI}]$) to expand throughout the LFP particle surfaces and form a CEI. Nevertheless, both electrodes showed enough levels of reversibility of lithiation/delithiation reactions for multiple decades of cycles.

3.3.3. Full-Cell Demonstration Using the Polymer-Binder-Free Cathode and an Intercalation-Type Anode

In this last experimental section, the compatibility of the polymer-binder-free LFP– $\text{Li}_x[\text{C}_2\text{mpyr}]_{1-x}[\text{FSI}]$ cathode with rechargeable batteries using a non-alkali-metal anode was evaluated. The stable cycling of such full cells is challenging as there are no excessive Li^+ sources available in the cells, which differs from the LMB configuration (where Li^+ ions can be provided from lithium metal excessively) discussed previously. To maximize the energy density and cyclability of the batteries, the use of graphite on the anode side is preferred. However, IL-based electrolytes often suffer from the poor cyclability of graphite, which requires an SEI-forming additive to facilitate the reversible Li^+ intercalation/deintercalation [62–64], or the constituent ions need to be modified [65]. Meanwhile, $\text{Li}_{0.10}[\text{C}_2\text{mpyr}]_{0.90}[\text{FSI}]$ is reportedly compatible with graphite and supports its stable cycling [38]. Therefore, the graphite– $\text{Li}_{0.10}[\text{C}_2\text{mpyr}]_{0.90}[\text{FSI}]$ anode was employed for full-cell measurements. As this electrode undergoes a large irreversible reaction at the first cycle [38], it was preconditioned in a solid-state half-cell, and then the preconditioned graphite– $\text{Li}_{0.10}[\text{C}_2\text{mpyr}]_{0.90}[\text{FSI}]$ anode was paired with fresh LFP–15w-Li0.10 in $\text{Li}_{0.50}[\text{C}_2\text{mpyr}]_{0.50}[\text{FSI}]$ for demonstration (see Section 2.4.1 for the detailed procedure of cell assembly).

Figure 5a shows the charge/discharge profile of a preconditioned graphite– $\text{Li}_{0.10}[\text{C}_2\text{mpyr}]_{0.90}[\text{FSI}] \mid \text{LFP}–15w\text{-Li0.10}$ cell at the first cycle. This full cell showed a discharge capacity compatible with battery tests of LFP– $\text{Li}_x[\text{C}_2\text{mpyr}]_{1-x}[\text{FSI}]$ cathodes in the LMB configuration (e.g., Figure 4e,f), but the Coulombic efficiency for the first cycle was only 58%. The poor Coulombic efficiency cannot be attributed only to the SEI formation on graphite, as this process is speculated to have almost progressed during the first three cycles in a half-cell configuration. Because the first Coulombic efficiency

of LFP– $\text{Li}_x[\text{C}_2\text{mpyr}]_{1-x}[\text{FSI}]$ cathodes was evaluated to be >98% (e.g., Figures 3c and 4e,f), this irreversible capacity of the full cell appears to be originated from the preconditioned graphite– $\text{Li}_{0.10}[\text{C}_2\text{mpyr}]_{0.90}[\text{FSI}]$ side. As $\text{Li}_{0.50}[\text{C}_2\text{mpyr}]_{0.50}[\text{FSI}]$ (coming from the interlayer) and $\text{Li}_{0.10}[\text{C}_2\text{mpyr}]_{0.90}[\text{FSI}]$ (in the graphite anode layer) are miscible, the low first Coulombic efficiency would imply a partial rupture of the pre-formed SEI on graphite, requiring the irreversible electrochemical reaction to rebuild it. The subsequent cycles showed improved Coulombic efficiency, but the achievable capacity decreased as the cycle number increased. This is likely to be because of the capacity mismatch between the preconditioned graphite– $\text{Li}_{0.10}[\text{C}_2\text{mpyr}]_{0.90}[\text{FSI}]$ anode and LFP–15w–Li0.10 developed with an increase in the cycle number.

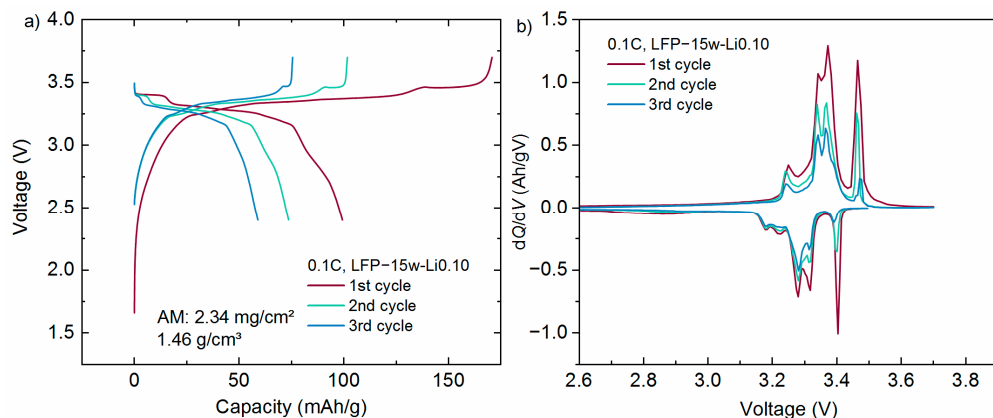


Figure 5. Full-cell demonstration of the polymer-binder-free LFP– $\text{Li}_{0.10}[\text{C}_2\text{mpyr}]_{0.90}[\text{FSI}]$ cathode (LFP–15w–Li0.10) paired with a preconditioned graphite– $\text{Li}_{0.10}[\text{C}_2\text{mpyr}]_{0.90}[\text{FSI}]$ anode in $\text{Li}_{0.50}[\text{C}_2\text{mpyr}]_{0.50}[\text{FSI}]$ at 50 °C. (a) The voltage profiles of a graphite– $\text{Li}_{0.10}[\text{C}_2\text{mpyr}]_{0.90}[\text{FSI}]$ | LFP–15w–Li0.10 cell for the first three cycles at 0.1C. (b) The dQ/dV profiles of the graphite– $\text{Li}_{0.10}[\text{C}_2\text{mpyr}]_{0.90}[\text{FSI}]$ | LFP–15w–Li0.10 cell for the first three cycle at 0.1C.

To provide further insights into the reversibility of electrochemical reactions on both electrodes, dQ/dV analysis was performed. Figure 5b depicts four dQ/dV peaks in the charge step and five dQ/dV peaks in the discharge step. A peak in this type of graph shows the equilibrium between different electrochemically active phases [66] and can inform the progress of electrochemical reactions on both electrodes separately if the two successive peaks are separated well. The narrow oxidation peak at 3.46 V would correspond to the deintercalation of Li^+ ions from LFP, while the reduction peak at 3.40 V would be the intercalation of Li^+ ions to LFP [53]. Another possibility for this redox couple is lithium plating/stripping at the (fully lithiated) graphite surface. On the other hand, the broader peaks at 3.24, 3.34, and 3.37 V for oxidation and 3.17, 3.28, and 3.32 V for reduction are related to the intercalation/deintercalation of Li^+ ions on the graphite side [53], and each pair of dQ/dV peaks is assigned to the transition from one stage structure to another [67,68]. The origin of the dQ/dV peak at 3.22 V for the reduction process has yet to be fully understood, but some types of graphite (e.g., mesocarbon microbeads) are known to show this additional dQ/dV peak during their delithiation [69–71]. From the comparison between the total area of dQ/dV processes during lithiation and that during delithiation for graphite, it was found that a large part of irreversible capacity was consumed on the graphite side at the full-cell voltage of 3.15–3.42 V, and the irreversible reaction was concurrent with multiple Li^+ ion intercalation steps of graphite. Conversely, the areas of the dQ/dV oxidation/reduction peaks at the highest voltage were almost the same as each other, suggesting the relatively good reversibility of this redox couple.

Although engineering the anode and electrolyte is required to improve the cyclability, this study successfully demonstrated the initial stage of the full-cell operation of

rechargeable batteries comprising the polymer-binder-free LFP– $\text{Li}_x[\text{C}_2\text{mpyr}]_{1-x}[\text{FSI}]$ cathode and graphite anode. This lays the strong foundation for future studies on OIPC-based batteries using a polymer-binder-free approach. Such batteries will be most likely to be solid-state batteries, thereby minimizing the structural-deformation-induced capacity decay of polymer-binder-free electrodes for better cyclability.

4. Conclusions

We created polymer-binder-free LFP electrodes using $\text{Li}_x[\text{C}_2\text{mpyr}]_{1-x}[\text{FSI}]$ as an ion-conductive binder. The highest $\text{Li}_x[\text{C}_2\text{mpyr}]_{1-x}[\text{FSI}]$ content of 50 wt% enabled the generation of homogeneous, crack-free, high-loading LFP electrodes with an achievable areal capacity of $>1.5 \text{ mAh/cm}^2$ (whose theoretical value can be further increased up to 3.74 mAh/cm^2 at 50 mol% Li^+ with the sacrificed mechanical stability of the composite electrode against roll pressing). On the other hand, the $\text{Li}_x[\text{C}_2\text{mpyr}]_{1-x}[\text{FSI}]$ -deficient condition (i.e., 15 wt% $\text{Li}_x[\text{C}_2\text{mpyr}]_{1-x}[\text{FSI}]$) provided the electrodes with a high LFP weight ratio and sufficient mechanical integrity at a low electrode-loading value. Therefore, such electrodes showed high charge/discharge rate capabilities, especially at a low Li^+ concentration: The 2C/0.1C capacity ratios were 97.2% at 1 mol% Li^+ and 81.4% at 50 mol% Li^+ for lithiation, and those were 94.6% at 1 mol% Li^+ and 76.5% at 50 mol% Li^+ for delithiation. We clarified that a polymer-binder-free approach can offer three benefits over a conventional approach using PVDF as a (non-conductive) binder for LFP: (i) a higher nominal areal capacity, (ii) a lower electrolyte amount for half-cell operation, and (iii) higher Coulombic efficiency, which implies further engineering of polymer-binder-free electrodes helps contribute to overcoming the performance limitations of electrodes imposed by non-conductive binders. A full cell using the polymer-binder-free LFP cathode and preconditioned graphite anode was successfully cycled several times, demonstrating the possibility of creating advanced LIBs (without lithium-metal anodes) via the polymer-binder-free approach.

These findings demonstrate the huge potential of OIPC–lithium salt mixtures as promising ion-conductive binders to create functional polymer-binder-free electrodes using existing fabrication processes for various types of LIBs (i.e., the one requiring the electrode’s high areal capacity as well as the one requiring fast charging/discharging capabilities). The exploration of OIPC–lithium salt mixtures as ion-conductive binders even opens up the possibility of employing this polymer-binder-free approach in solid-state batteries in the future (e.g., to address the compatibility issue of a conventional binder with a solid electrolyte).

Supplementary Materials: The following supporting information can be downloaded at <https://www.mdpi.com/article/10.3390/batteries11010003/s1>, Table S1: The details of the LFP electrodes used for battery tests. This helps explain the competitiveness of the polymer-binder-free approach together with the relevant information presented in Refs. [26,72–75]; Figure S1: The surfaces of polymer-binder-free LFP– $\text{Li}_x[\text{C}_2\text{mpyr}]_{1-x}[\text{FSI}]$ electrodes. (a) LFP–15w-Li0.01, (b) LFP–15w-Li0.10, (c) LFP–15w-Li0.50, (d) LFP–50w-Li0.01, (e) LFP–50w-Li0.10, and (f) LFP–50w-Li0.50; Figure S2: DSC heating traces of LFP– $\text{Li}_x[\text{C}_2\text{mpyr}]_{1-x}[\text{FSI}]$ at (a) the first scan and (b) the second scan. This helps explain the thermal behavior of LFP– $\text{Li}_x[\text{C}_2\text{mpyr}]_{1-x}[\text{FSI}]$ together with the relevant information presented in Refs. [31,34]; Figure S3: The charge/discharge profiles of the polymer-binder-containing LFP electrode (LFP–6w-PVDF) in LP30 (1 M LiPF_6 in EC–DMC, 50:50 vol%) and $\text{Li}_{0.50}[\text{C}_2\text{mpyr}]_{0.50}[\text{FSI}]$ at 0.1C, 50 °C; Figure S4: (a) Discharge capacity retentions and (b) Coulombic efficiencies of high-loading LFP–50w-Li0.01 and low-loading LFP–6w-PVDF cathodes in $\text{Li}_{0.50}[\text{C}_2\text{mpyr}]_{0.50}[\text{FSI}]$ for 13 cycles at 0.1C, 50 °C; Figure S5: The initial charge/discharge profiles of the thick polymer-binder-free LFP– $\text{Li}_{0.50}[\text{C}_2\text{mpyr}]_{0.50}[\text{FSI}]$ electrode (LFP–50w-Li0.50 with the nominal areal capacity of 2.65 mAh/cm^2) in $\text{Li}_{0.50}[\text{C}_2\text{mpyr}]_{0.50}[\text{FSI}]$ at 0.1C, 50 °C; Figure S6:

(a) Discharge capacity retentions and (b) Coulombic efficiencies of LFP–15w-Li0.01, LFP–15w-Li0.50, and LFP–6w-PVDF cathodes in $\text{Li}_{0.50}[\text{C}_2\text{mpyr}]_{0.50}[\text{FSI}]$ for 13 cycles at 0.1C, 50 °C.

Author Contributions: D.M.J., investigation, validation, formal analysis, data curation, writing—original draft, writing—review and editing, visualization; M.F., supervision; P.C.H., supervision; H.U., conceptualization, funding acquisition, project administration, supervision, investigation, validation, formal analysis, data curation, visualization, writing—original draft, writing—review and editing. All authors have read and agreed to the published version of the manuscript.

Funding: This project was part of the MESC master program, and this publication acknowledges funding from the European Commission Erasmus+. H.U. acknowledges the Alfred Deakin Postdoctoral Research Fellowship (ADPRF) at Deakin University for support.

Data Availability Statement: The original contributions presented in this study are included in the article/Supplementary Material. Further inquiries can be directed to the corresponding author.

Acknowledgments: We would like to thank Mohand Oumerabet (Bordeaux INP) for his assistance in conducting the electrode stability test (Figure 2g).

Conflicts of Interest: The authors declare no conflicts of interest.

References

- Zubi, G.; Dufo-López, R.; Carvalho, M.; Pasaoglu, G. The lithium-ion battery: State of the art and future perspectives. *Renew. Sustain. Energy Rev.* **2018**, *89*, 292–308. [[CrossRef](#)]
- Martins, L.S.; Guimarães, L.F.; Botelho Junior, A.B.; Tenório, J.A.S.; Espinosa, D.C.R. Electric car battery: An overview on global demand, recycling and future approaches towards sustainability. *J. Environ. Manag.* **2021**, *295*, 113091. [[CrossRef](#)] [[PubMed](#)]
- Hemavathi, S.; Srirama, S.; Prakash, A.S. Present and Future Generation of Secondary Batteries: A Review. *ChemBioEng Rev.* **2023**, *10*, 1123–1145. [[CrossRef](#)]
- Waseem, M.; Ahmad, M.; Parveen, A.; Suhaib, M. Battery technologies and functionality of battery management system for EVs: Current status, key challenges, and future prospectives. *J. Power Sources* **2023**, *580*, 233349. [[CrossRef](#)]
- Detka, K.; Górecki, K. Selected Technologies of Electrochemical Energy Storage—A Review. *Energies* **2023**, *16*, 5034. [[CrossRef](#)]
- Hannan, M.A.; Hoque, M.M.; Hussain, A.; Yusof, Y.; Ker, P.J. State-of-the-Art and Energy Management System of Lithium-Ion Batteries in Electric Vehicle Applications: Issues and Recommendations. *IEEE Access* **2018**, *6*, 19362–19378. [[CrossRef](#)]
- Ueda, H.; Yoshimoto, S. Multi-redox Active Carbons and Hydrocarbons: Control of their Redox Properties and Potential Applications. *Chem. Rec.* **2021**, *21*, 2411–2429. [[CrossRef](#)]
- Zu, C.; Ren, Y.; Guo, F.; Yu, H.; Li, H. A Reflection on Lithium-Ion Batteries from a Lithium-Resource Perspective. *Adv. Energy Sustain. Res.* **2021**, *2*, 2100062. [[CrossRef](#)]
- Manzetti, S.; Mariasiu, F. Electric vehicle battery technologies: From present state to future systems. *Renew. Sustain. Energy Rev.* **2015**, *51*, 1004–1012. [[CrossRef](#)]
- Chen, J.; Liu, J.; Qi, Y.; Sun, T.; Li, X. Unveiling the Roles of Binder in the Mechanical Integrity of Electrodes for Lithium-Ion Batteries. *J. Electrochem. Soc.* **2013**, *160*, A1502–A1509. [[CrossRef](#)]
- Ram, R.; Soni, V.; Khastgir, D. Electrical and thermal conductivity of polyvinylidene fluoride (PVDF)—Conducting Carbon Black (CCB) composites: Validation of various theoretical models. *Compos. Part B Eng.* **2020**, *185*, 107748. [[CrossRef](#)]
- Li, A.; Hempel, J.L.; Balogh, M.P.; Cheng, Y.-T.; Taub, A.I. Effect of Binder Content on Silicon Microparticle Anodes for Lithium-Ion Batteries. *J. Electrochem. Soc.* **2023**, *170*, 010533. [[CrossRef](#)]
- Gordon, R.; Kassar, M.; Willenbacher, N. Effect of Polymeric Binders on Dispersion of Active Particles in Aqueous LiFePO₄-Based Cathode Slurries as well as on Mechanical and Electrical Properties of Corresponding Dry Layers. *ACS Omega* **2020**, *5*, 11455–11465. [[CrossRef](#)] [[PubMed](#)]
- Liu, G.; Zheng, H.; Song, X.; Battaglia, V.S. Particles and Polymer Binder Interaction: A Controlling Factor in Lithium-Ion Electrode Performance. *J. Electrochem. Soc.* **2012**, *159*, A214–A221. [[CrossRef](#)]
- Kubarkov, A.V.; Babkin, A.V.; Drozhzhin, O.A.; Stevenson, K.J.; Antipov, E.V.; Sergeyev, V.G. Engendering High Energy Density LiFePO₄ Electrodes with Morphological and Compositional Tuning. *Nanomaterials* **2023**, *13*, 1771. [[CrossRef](#)] [[PubMed](#)]
- Yoon, J.; Lee, J.; Kim, H.; Kim, J.; Jin, H.-J. Polymeric Binder Design for Sustainable Lithium-Ion Battery Chemistry. *Polymers* **2024**, *16*, 254. [[CrossRef](#)] [[PubMed](#)]
- Liang, X.; Ahmad, N.; Zhang, B.; Zeng, C.; Cao, X.; Dong, Q.; Yang, W. Research progress of robust binders with superior mechanical properties for high-performance silicon-based lithium-ion batteries. *Mater. Chem. Front.* **2024**, *8*, 1480–1512. [[CrossRef](#)]

18. Qin, T.; Yang, H.; Li, Q.; Yu, X.; Li, H. Design of functional binders for high-specific-energy lithium-ion batteries: From molecular structure to electrode properties. *Ind. Chem. Mater.* **2024**, *2*, 191–225. [CrossRef]
19. Zhang, L.; Wu, X.; Qian, W.; Pan, K.; Zhang, X.; Li, L.; Jia, M.; Zhang, S. Exploring More Functions in Binders for Lithium Batteries. *Electrochem. Energy Rev.* **2023**, *6*, 36. [CrossRef]
20. Li, J.; Chen, X.; Muhammad, S.; Roy, S.; Huang, H.; Yu, C.; Ullah, Z.; Wang, Z.; Zhang, Y.; Wang, K.; et al. Development of Solid Polymer Electrolytes for Solid-State Lithium Battery Applications. *Mater. Today Energy* **2024**, *43*, 101574. [CrossRef]
21. Su, G.; Zhang, X.; Xiao, M.; Wang, S.; Huang, S.; Han, D.; Meng, Y. Polymeric Electrolytes for Solid-state Lithium Ion Batteries: Structure Design, Electrochemical Properties and Cell Performances. *ChemSusChem* **2023**, *17*, e202300293. [CrossRef] [PubMed]
22. Meng, N.; Ye, Y.; Yang, Z.; Li, H.; Lian, F. Developing Single-Ion Conductive Polymer Electrolytes for High-Energy-Density Solid State Batteries. *Adv. Funct. Mater.* **2023**, *33*, 2305072. [CrossRef]
23. Ueda, H. Interphase-driven ion conduction in organic ionic plastic crystal-based solid electrolytes: A review of symmetric cell studies. In *Encyclopedia of Solid-Liquid Interfaces*, 1st ed.; Wandelt, K., Bussetti, G., Eds.; Elsevier: Oxford, UK, 2024; pp. 743–775.
24. Hawley, W.B.; Li, J. Electrode manufacturing for lithium-ion batteries—Analysis of current and next generation processing. *J. Energy Storage* **2019**, *25*, 100862. [CrossRef]
25. Pringle, J.M. Recent progress in the development and use of organic ionic plastic crystal electrolytes. *Phys. Chem. Chem. Phys.* **2013**, *15*, 1339–1351. [CrossRef]
26. Zhou, Y.; Wang, X.; Zhu, H.; Armand, M.; Forsyth, M.; Greene, G.W.; Pringle, J.M.; Howlett, P.C. N-ethyl-N-methylpyrrolidinium bis(fluorosulfonyl)imide-electrospun polyvinylidene fluoride composite electrolytes: Characterization and lithium cell studies. *Phys. Chem. Chem. Phys.* **2017**, *19*, 2225–2234. [CrossRef] [PubMed]
27. Macfarlane, D.R.; Huang, J.; Forsyth, M. Lithium-doped plastic crystal electrolytes exhibiting fast ion conduction for secondary batteries. *Nature* **1999**, *402*, 792–794. [CrossRef]
28. Thomas, M.L.; Hatakeyama-Sato, K.; Nanbu, S.; Yoshizawa-Fujita, M. Organic ionic plastic crystals: Flexible solid electrolytes for lithium secondary batteries. *Energy Adv.* **2023**, *2*, 748–764. [CrossRef]
29. Ueda, H.; Saito, N.; Nakanishi, A.; Zhu, H.; Kerr, R.; Mizuno, F.; Howlett, P.C.; Forsyth, M. Unveiling the dynamic change in the ionic conductivity of a solid-state binary mixture comprising an organic ionic plastic crystal and LiBF₄. *Mater. Today Phys.* **2024**, *43*, 101395. [CrossRef]
30. Henderson, W.A.; Seo, D.M.; Zhou, Q.; Boyle, P.D.; Shin, J.-H.; De Long, H.C.; Trulove, P.C.; Passerini, S. An Alternative Ionic Conductivity Mechanism for Plastic Crystalline Salt-Lithium Salt Electrolyte Mixtures. *Adv. Energy Mater.* **2012**, *2*, 1343–1350. [CrossRef]
31. Zhou, Y.; Wang, X.; Zhu, H.; Yoshizawa-Fujita, M.; Miyachi, Y.; Armand, M.; Forsyth, M.; Greene, G.W.; Pringle, J.M.; Howlett, P.C. Solid-State Lithium Conductors for Lithium Metal Batteries Based on Electrospun Nanofiber/Plastic Crystal Composites. *ChemSusChem* **2017**, *10*, 3135–3145. [CrossRef] [PubMed]
32. Nti, F.; Ueda, H.; Kang, C.S.M.; Greene, G.W.; Pringle, J.M.; Zhu, H.; Howlett, P.; Forsyth, M.; Wang, X. Ion Transport in Li-Doped Triethyl(methyl)phosphonium Tetrafluoroborate (Li-[P₁₂₂₂][BF₄]) Impregnated with PVDF Nanoparticles. *J. Phys. Chem. C* **2022**, *126*, 3839–3852. [CrossRef]
33. Liang, Y.; Kerr, R.; Wang, X.; Ueda, H.; Armand, M.; Forsyth, M.; Howlett, P.C. New Plastic Crystal Composite Electrodes Employing Delocalized Transition Metal Salts for Low-Cost, High-Safety All-Solid-State Salt Batteries. *Chem. Mater.* **2024**, *36*, 7222–7231. [CrossRef]
34. Ueda, H.; Mizuno, F.; Forsyth, M.; Howlett, P.C. Tailoring Silicon Composite Anodes with Li⁺-Containing Organic Ionic Plastic Crystals for Solid-State Batteries. *J. Electrochem. Soc.* **2024**, *171*, 020556. [CrossRef]
35. Del Olmo, R.; Guzmán-González, G.; Sanz, O.; Forsyth, M.; Casado, N. Versatile mixed ionic-electronic conducting binders for high-power, high-energy batteries. *Electrochim. Acta* **2024**, *474*, 143547. [CrossRef]
36. Howlett, P.; Forsyth, M.; Kerr, R.; Mendes, T.; Ueda, H.; Liang, Y. Ionic Binders for Solid State Electrodes. WO 2023/019322 A1. 19 August 2022. Available online: <https://www.lens.org/lens/patent/182-776-638-310-197> (accessed on 15 November 2024).
37. del Olmo, R.; Mendes, T.C.; Forsyth, M.; Casado, N. Mixed ionic and electronic conducting binders containing PEDOT:PSS and organic ionic plastic crystals toward carbon-free solid-state battery cathodes. *J. Mater. Chem. A* **2022**, *10*, 19777–19786. [CrossRef]
38. Ueda, H.; Mizuno, F.; Kerr, R.; Forsyth, M.; Howlett, P.C. Fast Charge and High Stability of Solid-State Graphite Organic Ionic Plastic Crystal Composite Anodes. *Batter. Supercaps* **2022**, *5*, e202200057. [CrossRef]
39. Li, S.; Geng, Z.; Liu, L.; Wang-Lei, D.; Su, Q.; Liao, W. Wide-Temperature-Range Solid Electrolyte and Application Thereof. CN 113140787 A, 23 March 2021. Available online: <https://www.lens.org/lens/patent/101-108-149-362-437> (accessed on 15 November 2024).
40. Niu, H.; Wang, L.; Guan, P.; Zhang, N.; Yan, C.; Ding, M.; Guo, X.; Huang, T.; Hu, X. Recent Advances in Application of Ionic Liquids in Electrolyte of Lithium Ion Batteries. *J. Energy Storage* **2021**, *40*, 102659. [CrossRef]

41. Hwang, J.; Okada, H.; Haraguchi, R.; Tawa, S.; Matsumoto, K.; Hagiwara, R. Ionic liquid electrolyte for room to intermediate temperature operating Li metal batteries: Dendrite suppression and improved performance. *J. Power Sources* **2020**, *453*, 227911. [[CrossRef](#)]
42. Gao, X.; Wu, F.; Mariani, A.; Passerini, S. Concentrated Ionic-Liquid-Based Electrolytes for High-Voltage Lithium Batteries with Improved Performance at Room Temperature. *ChemSusChem* **2019**, *12*, 4185–4193. [[CrossRef](#)] [[PubMed](#)]
43. Yunis, R.; Al-Masri, D.; Hollenkamp, A.F.; Doherty, C.M.; Zhu, H.; Pringle, J.M. Plastic Crystals Utilising Small Ammonium Cations and Sulfonylimide Anions as Electrolytes for Lithium Batteries. *J. Electrochem. Soc.* **2020**, *167*, 070529. [[CrossRef](#)]
44. Yunis, R.; Newbegin, T.W.; Hollenkamp, A.F.; Pringle, J.M. Ionic liquids and plastic crystals with a symmetrical pyrrolidinium cation. *Mater. Chem. Front.* **2018**, *2*, 1207–1214. [[CrossRef](#)]
45. Preger, Y.; Barkholtz, H.M.; Fresquez, A.; Campbell, D.L.; Juba, B.W.; Romà-Kustas, J.; Ferreira, S.R.; Chalamala, B. Degradation of Commercial Lithium-Ion Cells as a Function of Chemistry and Cycling Conditions. *J. Electrochem. Soc.* **2020**, *167*, 120532. [[CrossRef](#)]
46. Mao, N.; Gadkari, S.; Wang, Z.; Zhang, T.; Bai, J.; Cai, Q. A comparative analysis of lithium-ion batteries with different cathodes under overheating and nail penetration conditions. *Energy* **2023**, *278*, 128027. [[CrossRef](#)]
47. Chen, J.; Whittingham, M. Hydrothermal synthesis of lithium iron phosphate. *Electrochem. Commun.* **2006**, *8*, 855–858. [[CrossRef](#)]
48. Henderson, W.A.; Young, V.G.; Passerini, S.; Trulove, P.C.; De Long, H.C. Plastic Phase Transitions in *N*-Ethyl-*N*-methylpyrrolidinium Bis(trifluoromethanesulfonyl)imide. *Chem. Mater.* **2006**, *18*, 934–938. [[CrossRef](#)]
49. Ramana, C.V.; Mauger, A.; Gendron, F.; Julien, C.M.; Zaghib, K. Study of the Li-insertion/extraction process in LiFePO₄/FePO₄. *J. Power Sources* **2009**, *187*, 555–564. [[CrossRef](#)]
50. Padhi, A.K.; Nanjundaswamy, K.S.; Goodenough, J.B. Phospho-olivines as Positive-Electrode Materials for Rechargeable Lithium Batteries. *J. Electrochem. Soc.* **1997**, *144*, 1188–1194. [[CrossRef](#)]
51. Kim, Y.; Kim, M.; Lee, T.; Kim, E.; An, M.; Park, J.; Cho, J.; Son, Y. Investigation of mass loading of cathode materials for high energy lithium-ion batteries. *Electrochem. Commun.* **2023**, *147*, 107437. [[CrossRef](#)]
52. Deng, W.; Yin, X.; Bao, W.; Zhou, X.; Hu, Z.; He, B.; Qiu, B.; Meng, Y.S.; Liu, Z. Quantification of reversible and irreversible lithium in practical lithium-metal batteries. *Nat. Energy* **2022**, *7*, 1031–1041. [[CrossRef](#)]
53. Torai, S.; Nakagomi, M.; Yoshitake, S.; Yamaguchi, S.; Oyama, N. State-of-health estimation of LiFePO₄/graphite batteries based on a model using differential capacity. *J. Power Sources* **2016**, *306*, 62–69. [[CrossRef](#)]
54. Homann, G.; Stoltz, L.; Nair, J.; Laskovic, I.C.; Winter, M.; Kasnatscheew, J. Poly(Ethylene Oxide)-based Electrolyte for Solid-State-Lithium-Batteries with High Voltage Positive Electrodes: Evaluating the Role of Electrolyte Oxidation in Rapid Cell Failure. *Sci. Rep.* **2020**, *10*, 4390. [[CrossRef](#)] [[PubMed](#)]
55. Lee, J.; Jeong, S.H.; Nam, J.S.; Sagong, M.; Ahn, J.; Lim, H.; Kim, I.D. Toward thin and stable anodes for practical lithium metal batteries: A review, strategies, and perspectives. *EcoMat* **2023**, *5*, e12416. [[CrossRef](#)]
56. Cheng, H.; Tan, R.; Li, J.; Huang, J.; Song, W. Coatings on Lithium Battery Separators: A Strategy to Inhibit Lithium Dendrites Growth. *Molecules* **2023**, *28*, 7788. [[CrossRef](#)] [[PubMed](#)]
57. Li, Y.; Sha, L.; Lv, P.; Qiu, N.; Zhao, W.; Chen, B.; Hu, P.; Zhang, G. Influences of Separator Thickness and Surface Coating on Lithium Dendrite Growth: A Phase-Field Study. *Materials* **2022**, *15*, 7912. [[CrossRef](#)]
58. Gogia, A.; Wang, Y.; Rai, A.K.; Bhattacharya, R.; Subramanyam, G.; Kumar, J. Binder-Free, Thin-Film Ceramic-Coated Separators for Improved Safety of Lithium-Ion Batteries. *ACS Omega* **2021**, *6*, 4204–4211. [[CrossRef](#)]
59. Rafiz, K.; Murali, D.R.L.; Lin, J.Y.S. Suppressing lithium dendrite growth on lithium-ion/metal batteries by a tortuously porous γ -alumina separator. *Electrochim. Acta* **2022**, *421*, 140478. [[CrossRef](#)]
60. Broadhead, J.; Kuo, H.C. Electrochemical Principles and Reactions. In *Handbook of Batteries*, 3rd ed.; Linden, D., Reddy, T.B., Eds.; The McGraw-Hill Companies, Inc.: New York, NY, USA, 2002.
61. Gabano, J.P.; Jumel, Y.; Laurent, J.F. A Potential-Time Study of the Mass Transfer Phenomena Due to the Lithium Ions in Non-Aqueous Electrolytes. In *Research and Development in Non-Mechanical Electrical Power Sources*; Collins, D.H., Ed.; Pergamon Press Inc.: Elmsford, NY, USA, 1970; pp. 255–265.
62. Sun, X.-G.; Dai, S. Electrochemical investigations of ionic liquids with vinylene carbonate for applications in rechargeable lithium ion batteries. *Electrochim. Acta* **2010**, *55*, 4618–4626. [[CrossRef](#)]
63. Lewandowski, A.; Świderska-Mocek, A. Properties of the graphite-lithium anode in *N*-methyl-*N*-propylpiperidinium bis(trifluoromethanesulfonyl)imide as an electrolyte. *J. Power Sources* **2007**, *171*, 938–943. [[CrossRef](#)]
64. Holzapfel, M.; Jost, C.; Prodi-Schwab, A.; Krumeich, F.; Würsig, A.; Buqa, H.; Novák, P. Stabilisation of lithiated graphite in an electrolyte based on ionic liquids: An electrochemical and scanning electron microscopy study. *Carbon* **2005**, *43*, 1488–1498. [[CrossRef](#)]
65. Guerfi, A.; Duchesne, S.; Kobayashi, Y.; Vijh, A.; Zaghib, K. LiFePO₄ and graphite electrodes with ionic liquids based on bis(fluorosulfonyl)imide (FSI)[−] for Li-ion batteries. *J. Power Sources* **2008**, *175*, 866–873. [[CrossRef](#)]
66. Safari, M.; Delacourt, C. Aging of a Commercial Graphite/LiFePO₄ Cell. *J. Electrochem. Soc.* **2011**, *158*, A1123. [[CrossRef](#)]

67. Zhang, H.; Yang, Y.; Ren, D.; Wang, L.; He, X. Graphite as anode materials: Fundamental mechanism, recent progress and advances. *Energy Storage Mater.* **2021**, *36*, 147–170. [[CrossRef](#)]
68. Asenbauer, J.; Eisenmann, T.; Kuenzel, M.; Kazzazi, A.; Chen, Z.; Bresser, D. The success story of graphite as a lithium-ion anode material—Fundamentals, remaining challenges, and recent developments including silicon (oxide) composites. *Sustain. Energy Fuels* **2020**, *4*, 5387–5416. [[CrossRef](#)]
69. Li, X.; Colclasure, A.M.; Finegan, D.P.; Ren, D.; Shi, Y.; Feng, X.; Cao, L.; Yang, Y.; Smith, K. Degradation mechanisms of high capacity 18650 cells containing Si-graphite anode and nickel-rich NMC cathode. *Electrochim. Acta* **2019**, *297*, 1109–1120. [[CrossRef](#)]
70. Abd Elhamid Mahmoud, H.; Xiao, X.; Cai, M.E.I. Multifunction Battery Separator. US 2015/0147641 A1, 22 November 2013. Available online: <https://www.lens.org/lens/patent/010-146-986-292-526> (accessed on 15 November 2024).
71. Kim, J.-H.; Pieczonka, N.P.W.; Li, Z.; Wu, Y.; Harris, S.; Powell, B.R. Understanding the capacity fading mechanism in $\text{LiNi}_{0.5}\text{Mn}_{1.5}\text{O}_4$ /graphite Li-ion batteries. *Electrochim. Acta* **2013**, *90*, 556–562. [[CrossRef](#)]
72. Apachitei, G.; Hidalgo, M.; Dogaru, D.; Lain, M.; Heymer, R.; Marco, J.; Copley, M. Optimisation of Industrially Relevant Electrode Formulations for LFP Cathodes in Lithium Ion Cells. *Batteries* **2023**, *9*, 192. [[CrossRef](#)]
73. Wang, X.; Zhu, H.; Greene, G.W.; Zhou, Y.; Yoshizawa-Fujita, M.; Miyachi, Y.; Armand, M.; Forsyth, M.; Pringle, J.M.; Howlett, P.C. Organic Ionic Plastic Crystal-Based Composite Electrolyte with Surface Enhanced Ion Transport and Its Use in All-Solid-State Lithium Batteries. *Adv. Mater. Technol.* **2017**, *2*, 1700046. [[CrossRef](#)]
74. Hasa, I.; Mariyappan, S.; Saurel, D.; Adelhelm, P.; Koposov, A.Y.; Masquelier, C.; Croguennec, L.; Casas-Cabanas, M. Challenges of today for Na-based batteries of the future: From materials to cell metrics. *J. Power Sources* **2021**, *482*, 228872. [[CrossRef](#)]
75. Freiberg, A.; Metzger, M.; Haering, D.; Bretzke, S.; Puravankara, S.; Nilges, T.; Stinner, C.; Marino, C.; Gasteiger, H.A. Anodic Decomposition of Trimethylboroxine as Additive for High Voltage Li-Ion Batteries. *J. Electrochem. Soc.* **2014**, *161*, A2255. [[CrossRef](#)]

Disclaimer/Publisher’s Note: The statements, opinions and data contained in all publications are solely those of the individual author(s) and contributor(s) and not of MDPI and/or the editor(s). MDPI and/or the editor(s) disclaim responsibility for any injury to people or property resulting from any ideas, methods, instructions or products referred to in the content.